Raco Wind at the Exit of the Maipo Canyon in Central Chile: Climatology, Special Observations, and Possible Mechanisms

RICARDO C. MUÑOZ,[a] LAURENCE ARMI,[b] JOSÉ A. RUTLLANT,[a,c] MARK FALVEY,[a,d] C. DAVID WHITEMAN,[e] RENÉ GARREAUD,[a,f] ANDRÉS ARRIAGADA,[a,d] FEDERICO FLORES,[d] AND NICOLÁS DONOSO[d,g]

[a] *Department of Geophysics, University of Chile, Santiago, Chile*
[b] *Institute of Geophysics and Planetary Physics, Scripps Institution of Oceanography, La Jolla, California*
[c] *Center for Advanced Studies in Arid Zones, La Serena, Chile*
[d] *Meteodata Ltd., Santiago, Chile*
[e] *Department of Atmospheric Sciences, University of Utah, Salt Lake City*
[f] *Center for Climate and Resilience Research, Santiago, Chile*

(Manuscript received 3 August 2019, in final form 5 February 2020)

ABSTRACT

Raco is the local name given to a strong (gusts up to 17 m s^{-1}), warm, and dry down-valley wind observed at the exit of the Maipo River Canyon in central Chile. Its climatology is documented based on eight years of surface measurements near the canyon exit together with a more complete characterization of its structure during an intensive observational period (IOP) carried out in July 2018. Raco winds occur in the cold season under well-defined synoptic conditions, beginning abruptly at any time during the night, reaching maximum hourly averages around 10 m s^{-1}, and terminating around noon with the onset of afternoon westerly up-valley winds. About 25% of the days in May–August have more than six raco hours between 0100 and 1200 LT, and raco episodes last typically 1–2 days. The sudden appearance of raco winds at the surface can be accompanied by conspicuous warming (up to 10°C) and drying (up to 3 g kg^{-1}). Raco winds are associated with a strong along-canyon pressure gradient, a regional pressure fall, and clear skies. During the IOP, radiosondes launched from both extremes of the canyon exit corridor showed a nocturnal easterly jet at 700 m AGL that occasionally descended rapidly to the surface, producing the raco. Transects along the canyon performed with a mobile ceilometer revealed a sharp frontlike feature between the cold pool over the Santiago Valley and the raco-affected conditions in the Maipo Canyon. Possible factors producing the easterly jet aloft and its occasional descent toward the surface are discussed, and a gap-wind mechanism is postulated to be at work.

1. Introduction

The interaction of atmospheric flow with topography produces a great variety of phenomena on an ample range of temporal and spatial scales. In many cases, this interaction has effects that can be hazardous due to the intensity and gustiness of the resulting winds and wind shears, or, on the contrary, topographically induced stagnation and blocking can exacerbate air pollution in certain regions. Chile offers a privileged venue to study these flow–topography interactions in complex terrain, as the tall Andes Mountains run all along its eastern border, rising in the central part of the country to mean altitudes over 4000 m above sea level (MSL) at distances not more than 200 km from the Pacific Ocean (Fig. 1). Thus, the relief map in the region contains an assortment of topographic structures including coastal mountains, inland valleys, isolated peaks, transverse canyons intruding into the Andes Mountains, etc., all of them overlooked by the large Andes massif to the east. One manifestation of regional flow–terrain interaction is the occurrence of episodic strong down-valley (easterly) winds along the foothills of the Andes Cordillera, which, depending on the region, are known locally as ''terral'' (~30°S), ''raco'' (~33°S), and ''puelche'' (~35°–40°S).

Supplemental information related to this paper is available at the Journals Online website: https://doi.org/10.1175/JAMC-D-19-0188.s1.

[g] Current affiliation: Centro de Estudios Científicos, Valdivia, Chile.

Corresponding author: Ricardo C. Muñoz, rmunoz@dgf.uchile.cl

DOI: 10.1175/JAMC-D-19-0188.1

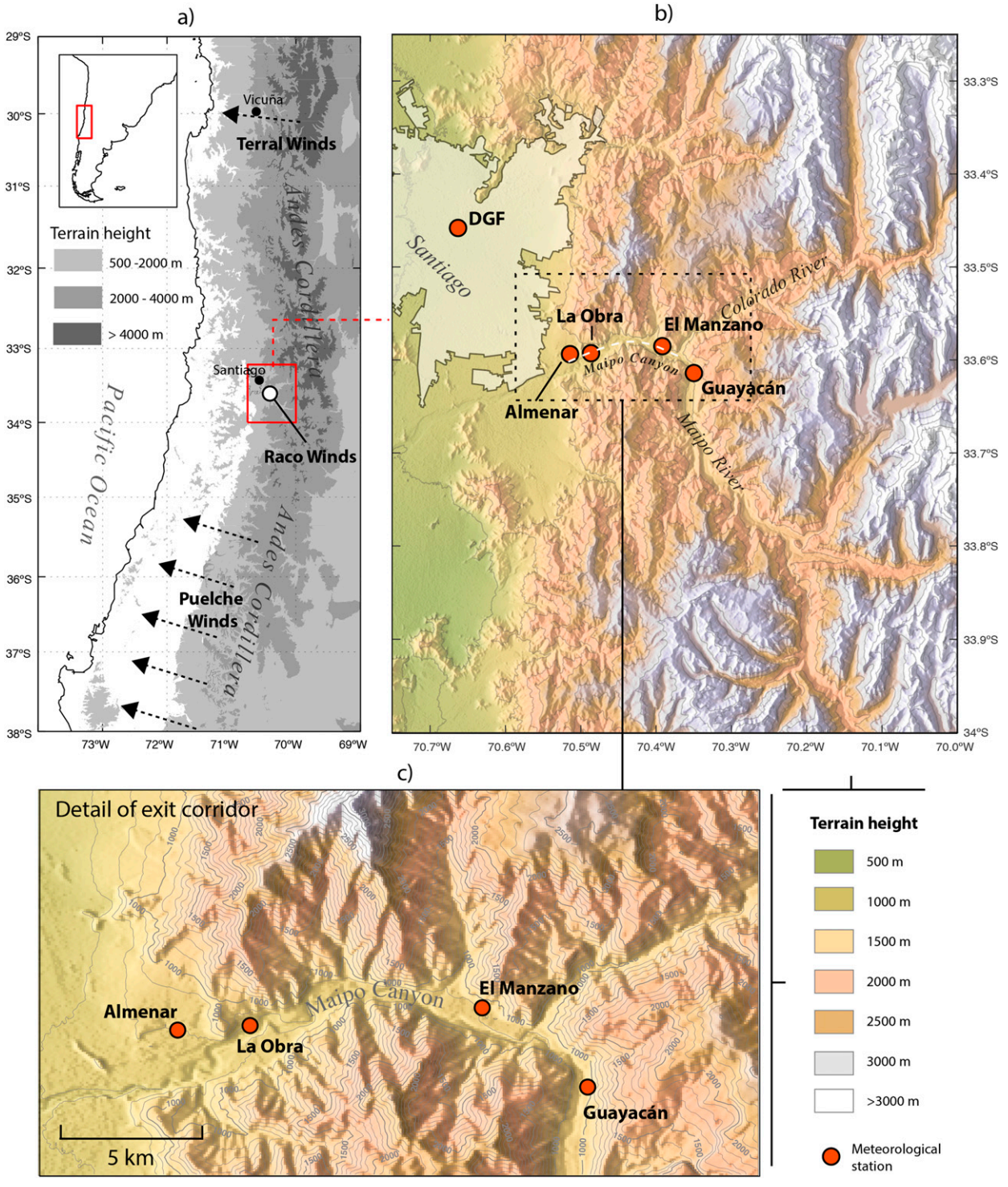

FIG. 1. (a) Topography of central Chile and its location in South America (inset). (b) Maipo River drainage network and easterly portion of Santiago Valley. Red circles mark sites with data used in the paper: Department of Geophysics (DGF) in downtown Santiago, Almenar (ALM), La Obra (LOB), El Manzano (MAN), and Guayacán (GUA). (c) Close-up of Maipo Canyon exit corridor.

Scientific studies have recently begun addressing these local winds, although to date emphasis has been placed on the large-scale synoptic patterns affecting their occurrence (Rutllant and Garreaud 2004; Montes et al. 2016; Montecinos et al. 2017). Besides their intensity, these winds have been variously related to fire hazards (Inzunza 2009), air pollution (Rutllant and Garreaud 2004), dust events (Arriagada 2019), and agriculture impacts (Montes et al. 2016).

Raco is the name given by the locals to a relatively strong (gusts up to 17 m s^{-1}), warm, and dry down-valley wind affecting the Maipo River Canyon in the southeastern region of Santiago's valley in central Chile, at the foothills of the Andes Cordillera (Fig. 1), which at these latitudes reaches heights above 5000 m MSL. Rutllant and Garreaud (2004, hereafter RG2004) presented the first documentation of basic climatological aspects of raco winds making use of four years of surface observations at El Manzano and one year at La Obra stations (see locations in section 2). According to their results, raco winds occur mainly in the cold season, have a marked synoptic-scale variability, and are mostly felt at the surface during nighttime and early morning hours. Applying a threshold to the dawn El Manzano wind speed data in order to define raco days, they concluded that during winter, raco episodes occur about once per week and have typical durations of 1–2 days. A concomitant anomalous warming associated with the raco wind was documented to reach up to about 8°C at El Manzano, which was hypothesized to be due to the destruction of the surface radiative inversion by the strong winds and the subsequent downward mixing of warmer air from aloft. Based upon 0800, 1100, and 1400 LT pilot balloons launched from La Obra in several raco cases, RG2004 showed also that raco surface winds are accompanied by a low-level easterly jet aloft with maximum speeds around 10 m s^{-1} in the first 100–300 m layer above the surface. Beyond this observational characterization, RG2004 also addressed the synoptic-scale features associated with raco events. In the majority (80%) of cases, the strong surface easterly winds were linked to lower-tropospheric easterly flow ensuing from postfrontal conditions closely tied to the development of coastal low systems, which are a major modulating factor of the weather in central Chile (Garreaud et al. 2002; Garreaud and Rutllant 2003). At midlevels around the Andes crest, preridge conditions sustain southwest winds precluding flow from crossing the Andes from the east, except in a few cases in which the ridge axis has a significant northwest–southeast tilt. The remaining 20% of cases were associated with prefrontal conditions, as a midlatitude depression approaches the coast of central Chile, and pretrough conditions with northwest winds prevail aloft. Both synoptic conditions imply a rapid lowering of surface pressure to the west of our study region, which will be deemed significant in our discussion section.

As mentioned earlier, two other locally renowned easterly winds in Chile are the terral and the puelche winds, which occur around 30°S and in the region between 35° and 40°S, respectively (Fig. 1). Montes et al. (2016) provided a climatology of terral events using surface data available at the Vicuña station located in the mid–upper section of the Elqui Valley. Defining terral hours with a criterion based upon wind speed, wind direction, air temperature, and relative humidity, they show that terral is mostly a cold-season phenomenon (April to August), occurs typically 6–7 times per season, and has a typical duration of 6–9 h, and its synoptic forcing is usually a migratory cold anticyclone to the south moving eastward, similar to what RG2004 found for the raco. Puelche winds, on the other hand, are more regional in scale and are not restricted to the winter season. While sharing a similar synoptic setting with both raco and terral, the easterly flow during puelche events is generally observed throughout the lower troposphere, crossing the Andes from Argentina. The warming and drying associated with puelche events appear to be due to the topographically induced subsidence connected to this easterly flow (Montecinos et al. 2017; Beusch et al. 2018).

Physical mechanisms by which terrain affects wind flow are commonly separated in two broad categories: thermodynamic and dynamic (Whiteman 2000). The former corresponds to horizontal pressure gradients arising from differential heating or cooling rates occurring over a topographic complex due to sloped surfaces, differences in terrain orientations, spatial changes of the terrain geometry, etc. By their very nature, these effects normally present a strong diurnal cycle, with resulting near-surface winds exhibiting opposite directions during daytime and nighttime. Moreover, while some particular synoptic patterns may strengthen one or the other diurnal phase of these winds, their evolution is best observed under weak large-scale forcing. Examples of thermodynamically driven winds that can be relevant in the raco case are katabatic winds and down-valley winds. The former refer to nocturnal flows over an inclined surface as the air in contact with the ground cools, and a negative buoyancy force accelerates the air parcels down the surface slope (Mahrt 1982). Intense katabatic winds have been reported over regions with large extensions of sloped surfaces subject to strong or long cooling periods, like the Antarctic continent or the Atacama Desert (Parish and Bromwich 1987; Muñoz et al. 2013). In less extreme settings, however, katabatic

winds are typically weak, although they may provide the supply of air for the other thermodynamically driven flow of interest here, the down-valley wind. In this case, the stronger cooling of the valley air mass as compared to that of the adjacent plain produces an along-valley pressure gradient that forces the air out of the valley during the night. This outflow usually takes the shape of a low-level jet, which at the exit of the valley may intensify and descend to the surface in what is known as a valley exit jet (Zardi and Whiteman 2013; Chrust et al. 2013).

Dynamic effects of terrain on wind flow, on the other hand, are also the result of topography-induced pressure gradients, but these arise not from differential heating or cooling but from the mechanical interaction between the flow and the underlying complex surface. Jackson et al. (2013) have provided a recent theoretical and observational review of dynamically forced phenomena, including downslope windstorms and gap winds, among others. Intense, warm and dry downslope winds at the lee side of a mountain barrier are commonly referred to as foehn winds. As illustrated by Richner and Hächler (2013) for a case in the Alps, the valley stations impacted by the foehn suffer an abrupt and sudden increase in wind speed together with simultaneous significant increases in temperature and drops in humidity. While several mechanisms have been proposed for this phenomenon, most attribute these observations to the arrival of air parcels that have been forced to descend by the mechanical interaction of the incoming flow with the mountain barrier. Besides the Alps, foehn-type winds have been documented downwind of many mountain barriers (e.g., Armi and Mayr 2011; Vüllers et al. 2018; Norte et al. 2008).

Another dynamical mechanism that may be relevant for the raco are gap winds. Instead of the vertical obstacle that air parcels encounter in the foehn case, gap winds arise when their path approaches a topographic lateral constriction in the form of a channel, a corridor, a narrows, or a mountain gap (Jackson et al. 2013, and references therein). Differences in air masses at both sides of the gap (Finn et al. 2016) or large-scale pressure gradients (Whiteman and Doran 1993; Mass et al. 2014) can force air parcels to accelerate along the gap reaching the highest velocities at the exit or closely downwind. This increase in kinetic energy of the air parcels is compensated by a decrease in potential energy due to a forced descent (Mayr et al. 2007). In foehn and gap winds, so-called hydraulic models have been successfully applied to understand their dynamics, which to a first approximation resemble the problem of a sloped open-channel water flow subject to variations in its bottom or lateral walls (Baines 1995). In the case of gap flows, hydraulic models have been extended to consider a continuously stratified flow approaching a channel constriction. An analytical self-similar solution of the problem was presented by Wood (1968), reproduced by laboratory experiments by Armi and Williams (1993), and applied in the understanding of so-called shallow-foehn cases by Armi and Mayr (2007).

As we shall argue in following sections, observations of the raco wind at the exit of the Maipo Canyon in central Chile share some aspects of valley exit jets, foehn, and gap winds. In this regard, a relevant study is that of Chrust et al. (2013, hereafter CWH2013), who investigated the wind jet at the exit of Weber Canyon, Utah, in a topographic setting remarkably similar to that of the Maipo Canyon in central Chile. Based on their observations, they find the jet to be thermodynamically driven by the cooling of the in-canyon air mass combined with descent, acceleration, and thinning of the flow as it exits the canyon. Similarities and differences between winds at these two canyons will be discussed in this paper with the aim of shedding light on the possible mechanisms behind the raco wind.

While RG2004 provided the first scientific documentation of raco winds and their synoptic-scale environment, some questions were left open; for example, a more comprehensive observational characterization of raco winds and their vertical and along-the-canyon variability and the nature of the smaller-scale orography effect on the flow. We address these issues by documenting with more detail the climatology and characteristics of raco winds using multiyear surface records and special intensive observational campaigns. Attention is shifted, though, to the La Obra station, which now has seven years of measurements and where the raco wind, temperature, and humidity signatures are stronger. Indeed, by considering mainly winds at El Manzano and showing time series averaged over many raco episodes, a distinctive feature of raco winds, namely, their very abrupt and sudden appearance at the surface, was only briefly commented on by RG2004. Section 2 of the paper describes the topographic and climatic setting of raco winds, the long-term observations available and the special observation periods. Section 3 documents the climatology of raco winds at La Obra and their covariability with winds elsewhere in the canyon and with pressure and cloudiness. Section 4 presents the results of an intensive observational period (IOP) carried out in July 2018. Section 5 discusses the results in the context of the possible mechanisms underlying the observations, and section 6 provides a summary of the results and some conclusions.

2. Orography, climate, and data

The study region is located in central Chile (Fig. 1a) around 33.5°S, in the Maipo Valley. The Maipo is the

TABLE 1. Automated meteorological stations used in the study.

Site	Period	Measurements (Heights)
La Obra Lat: 33.5914°S Lon: 70.4853°W Alt: 800 m MSL	Period 1: May 2001–May 2005 Period 2: April 2015–current (gap in Feb–Jul 2016)	Wind speed and wind direction (4 m AGL) Temperature and relative humidity (3 m AGL) Atmospheric pressure (1 m AGL) Solar radiation (3 m AGL)
El Manzano Lat: 33.5861°S Lon: 70.3911°W Alt: 907 m MSL	Period 1: Jun 1997–Dec 2013 Period 2: Jun 2018–current	Wind speed and wind direction (10 m AGL) Temperature and relative humidity (2 m AGL) Atmospheric pressure (1 m AGL, only in period 2)
Almenar Lat: 33.5939°S Lon: 70.5144°W Alt: 793 m MSL	Nov 2017–current	Wind speed and wind direction (6 m AGL) Temperature and relative humidity (2 m AGL) Atmospheric pressure (1 m AGL)
Guayacán Lat: 33.6153°S Lon: 70.3506°W Alt: 928 m MSL	2013–current	Wind speed and wind direction (10 m AGL) Temperature and relative humidity (2 m AGL) Atmospheric pressure (2 m AGL)
Department of Geophysics Lat: 33.4573°S Lon: 70.6618°W Alt: 548 m MSL	2004–current	Wind speed and wind direction (roof top, ~30 m AGL) Temperature and relative humidity (roof top) Atmospheric pressure (roof top) Solar radiation (roof top) Precipitation (roof top)

principal river in the region, running for about 250 km from its headwaters (~3000 m MSL) at the foot of the Maipo Volcano (34.16°S, 69.83°W, 5856 m MSL) down to its outlet to the Pacific near the town of Santo Domingo (33.62°S, 71.63°W). The upper section of the river cuts through the complex relief of the Andes Cordillera in what will be referred to as the Maipo Canyon (Fig. 1b). The latter has mostly a southeast–northwest orientation, except near its end where, after joining the Colorado River arriving from the east-northeast, it exits the mountains and flows westward toward the Santiago Valley through a zonally oriented 12 km corridor between El Manzano and La Obra (Figs. 1c and 16a). This exit corridor is a rather deep V-shaped passage that at its narrowest part has a width of about 7 km at about 800 m above the valley floor. The climate of the region is largely defined by the moderating influence of the semipermanent southeast Pacific anticyclone, providing for a very stable lower troposphere. During winter, however, the path of midlatitude weather systems moves northward along with the equatorward drift of the subtropical anticyclone and a stronger synoptic variability affects Santiago, producing rain events that account for most of the annual precipitation ranging between 200 and 700 mm (Garreaud 2013). In the mesoscale, under synoptically unperturbed conditions, the Santiago Valley shows a valley–mountain breeze regime characterized by moderate southwest winds in the afternoon and weak downslope easterly winds during the night (RG2004; Muñoz and Corral 2017). Further aloft, the climatological westerlies are blocked below about 600 hPa by the Andes resulting in a persistent northerly barrier jet existing above the valley–mountain circulation (RG2004; Kalthoff et al. 2002). These conditions are synoptically modulated by the recurrent development of coastal lows moving from north to south along the Pacific coast that cause the Santiago Valley to alternate between very stable, dry, and subsidence-enhanced conditions and less stable conditions in which the marine boundary layer penetrates into the inland valleys (Garreaud et al. 2002; Garreaud and Rutllant 2003).

Surface meteorological observations are detailed in Table 1, with site locations shown in Fig. 1b. The main station for this study, La Obra, is at the exit of the Maipo Canyon at 800 m MSL. Measurements there were made during two periods: from 2001 to 2005 and from 2015 onward. Instruments and their specific siting are comparable in both periods and only small biases in atmospheric pressure (2.5 hPa), relative humidity (2%), and wind direction (10°) were corrected to homogenize the datasets (not shown). The other two stations measuring raco winds are El Manzano and Almenar. The former has two measurement periods (1997–2013 and from June 2018 onward) while the latter was installed at the end of 2017 to collect data during IOPs. These two

TABLE 2. Instrumentation available in July 2018 special observation period.

System	Location	Details
Radiosondes	Almenar and El Manzano	6-hourly and additional launches when needed. InterMet iMet-4 radiosondes.
Sodar	Almenar	Scintec MFAS sodar. Vertical resolution: 25 m, time resolution: 15 min, range: 0–1000 m AGL (nominal).
Mobile ceilometer	29 transects along the canyon.	Vaisala CL31 ceilometer. Accompanying measurements of surface temperature, relative humidity, pressure, and GPS position made with InterMet iMet-XQ sensor.

stations are used to describe the spatial variability of raco winds along the canyon. Finally, the station at Guayacán is used to evaluate pressure gradients inside the canyon and a station at the Department of Geophysics (DGF) serves as a Santiago Valley station not directly influenced by the Maipo Canyon exit flow.

To more completely characterize the dynamic and thermodynamic structure of the lower troposphere under raco events, two special IOPs were carried out, one in September 2017 and another in July 2018. We focus here on the second IOP since it had a more complete array of instruments and more observational locations than the first, although the main characteristics of the phenomenon were observed to be similar in both cases. The second IOP was carried out in the Maipo Canyon from 1200 LT 22 July to 1200 LT 26 July 2018. Special observations included 1) radiosonde launches at Almenar and El Manzano; 2) continuous sound detection and ranging (sodar) operation at Almenar; and 3) a mobile ceilometer measuring transects along the canyon of the vertical distribution of aerosols together with surface measurements of temperature and humidity. More details of these observations are presented in Table 2.

3. Climatology

To help illustrate some key aspects of raco winds, Fig. 2 shows example time series at La Obra during the period from 19 to 26 July 2018 (days 22 to 26 cover the period with special observations described in section 4). The upper panel of Fig. 2 shows wind speed (VRACO) as projected along the raco wind direction (57°, to be justified shortly), so that high positive values are associated with raco winds. The raco wind has a very episodic character with low speeds less than $1\,m\,s^{-1}$ changing abruptly to a high-intensity mode with speeds generally surpassing $5\,m\,s^{-1}$ and reaching up to $10\,m\,s^{-1}$, as, for example, in the nights and dawns of days 21 and 23–26 July. While having a preference for nocturnal and early morning hours, these raco events have a synoptic-scale variability that modulates their timing, intensity, and duration and even makes them absent for some days. The sudden increases of wind speed are accompanied by conspicuous and simultaneous increases in temperature and decreases in water vapor content as shown in Figs. 2b and 2c. At the onset of a raco event air temperatures jump by 5°–10°C, which is quite significant given that this warming occurs at the beginning or in the middle of rather cold winter nights. At the same time, water vapor mixing ratio decreases to around $1\,g\,kg^{-1}$ and relative humidity drops to 5%–10% (not shown). To better appreciate these thermodynamic changes, Figs. 2b and 2c also show temperature and water vapor mixing ratio at station DGF located in the Santiago Valley but far from the Maipo Canyon exit (Fig. 1b). The diurnal cycles in temperature and water vapor at this site are typical for a subtropical valley station with daytime warming, nocturnal cooling, and low variability in water vapor mixing ratio. While the nonraco temperature and mixing ratio at La Obra closely match the corresponding values at DGF, the raco conditions at La Obra are clearly distinct from those in the valley.

A broader view of raco winds is presented in Fig. 3 in which hourly VRACO values are shown for the full year 2017. The figure is comparable to Fig. 4 of CWH2013, which shows a similar plot of the along-canyon wind speed measured at the exit of Weber Canyon in Utah, with the exception of the wind speed scale range, which has been reduced in order to account for the very different wind measuring heights of both cases [4 m vs 50 m above ground level (AGL)]. As in CWH2013, the strong down valley winds in our case occur mostly during the night and tend to persist several hours after sunrise. The seasonality and episodic character of raco winds are clear from Fig. 3. Stronger nocturnal winds occur mainly in the cold season, and five or six episodes stand out for their greater intensity, interspersed between nights of weaker winds. These features contrast with those of the CWH2013 case, in which the strong nocturnal winds occur year-round and maximum intensities are observed in summer and early fall. Different measuring heights or mechanisms at work could explain these contrasts.

a. *Raco hours, events, and episodes*

The joint frequency distribution of hourly wind speed and wind direction at La Obra is presented in Fig. 4a for

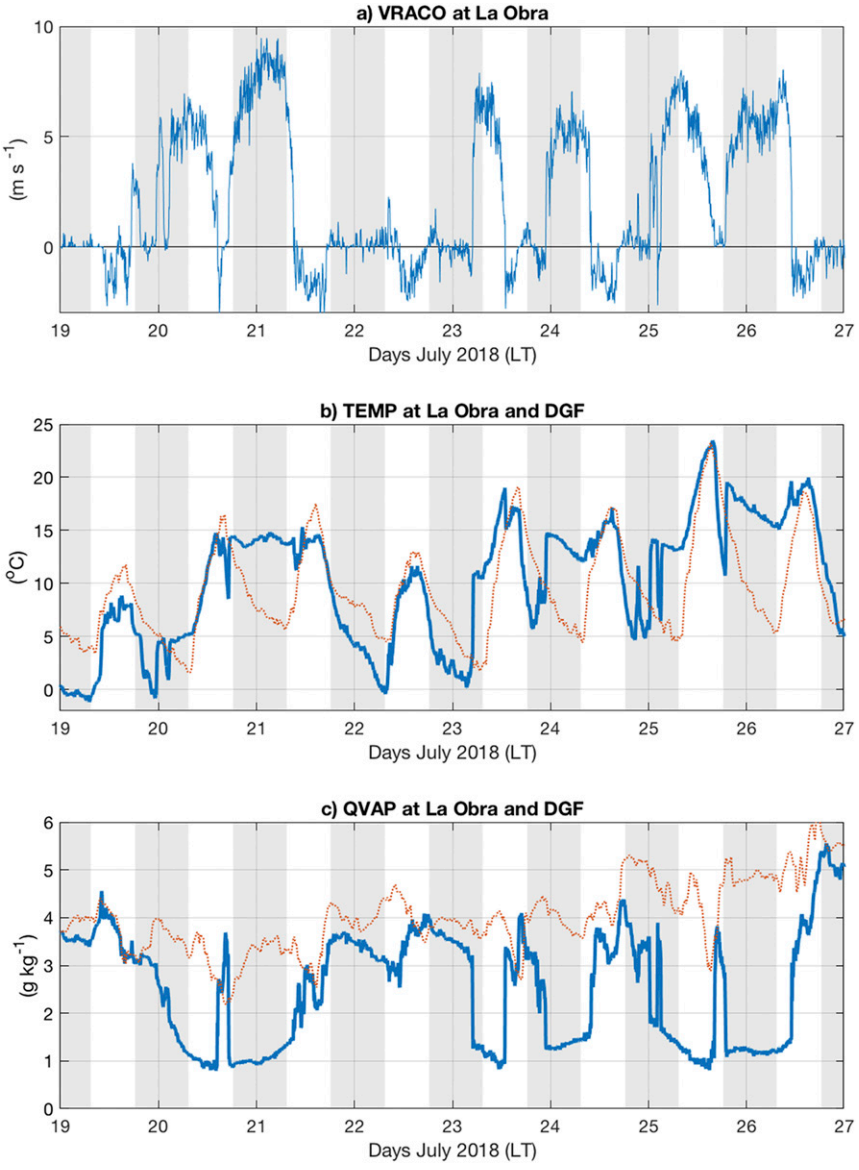

FIG. 2. (a) Time series of 5-min wind speed at La Obra projected along the raco wind direction (high positive values are associated with raco winds) for the period from 19 to 26 Jul 2018. Day marks indicate 0000 LT (UTC − 4) of the corresponding day. Shades indicate nocturnal periods. (b) As in (a), but for air temperature at stations La Obra (continuous blue line) and DGF (dotted red line). (c) As in (b), but for water vapor mixing ratio.

the full period of record. Three local maxima can be seen in this distribution: 1) southwesterly (~240°) wind direction with speeds up to $4\,m\,s^{-1}$ corresponding to afternoon up-valley flow that is more intense and frequent during summer; 2) very weak northerly (~0°) winds that occur during the night and are more frequent in summer; and 3) relatively intense northeasterly (~60°) winds with magnitudes reaching up to $9\,m\,s^{-1}$. The latter are recognized as raco winds, and their most frequent direction of 57° is used to define the raco intensity variable VRACO, as described in the previous section. Figure 4b shows the hourly and monthly frequency of VRACO $\geq 4\,m\,s^{-1}$, which is considered to be a reasonable threshold for moderate and strong raco events (see below). Consistent with Fig. 3, raco winds are clearly a nocturnal wintertime phenomenon with maximum frequency around daybreak in the months of June and July. During the afternoon and in the summer, raco winds are generally not observed at La Obra. Figure 4c shows the histogram of VRACO for hours 0600–0800 LT

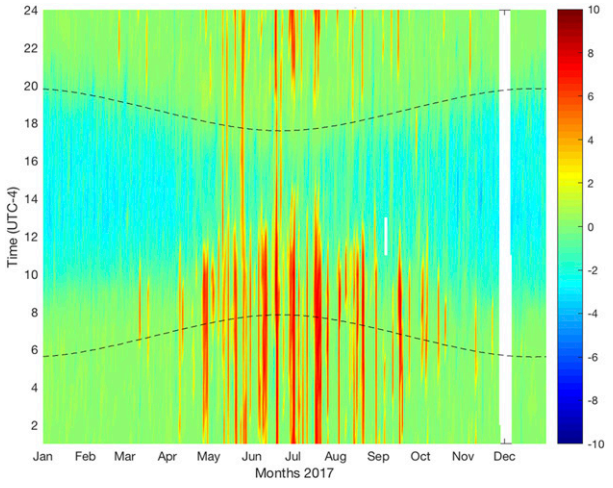

FIG. 3. Annual evolution of hourly wind speed ($m\,s^{-1}$) at La Obra projected along the raco wind direction for year 2017. Dashed lines indicate astronomical sunrise and sunset times.

between May and August. A bimodal distribution is observed, with a maximum frequency near zero and a broad secondary maximum with magnitudes greater than about $4\,m\,s^{-1}$. This bimodality was also documented by RG2004 and used by them to choose a threshold of $5\,m\,s^{-1}$ at El Manzano to define raco conditions. In our case, we have selected a VRACO threshold of $4\,m\,s^{-1}$ at La Obra to define raco hours, which amount to about 20% of the total number of hours in the months from May to August. Figure 4a suggests that even a threshold of $3\,m\,s^{-1}$ could have also been a plausible choice, in which case the raco frequencies documented later in this section (Fig. 7) would be higher. Methods to distinguish foehnlike winds from other downslope winds often make use of more variables than just wind speed and also consider temperature and humidity (Mayr et al. 2018; Montes et al. 2016; Montecinos et al. 2017). In our case, however, the high wind speed mode in the distribution shown in Fig. 4a is so clearly separated from the other modes in terms of magnitude and direction, that it was deemed unnecessary to add a priori other variables in the method used to define raco conditions. This approach allows us to subsequently examine more generally the relationship between raco winds and temperature, humidity, and other variables.

We define a raco event as a group of successive raco hours. Successive events separated by three or fewer hours or with VRACO in the intermediate hours not falling below $2\,m\,s^{-1}$ are subsequently merged into a single raco event. This method produces a total of 467 events for the months of May to August over the full period of record at La Obra (~8 years). For each event, their timing, duration, intensity, and concomitant initial and ending temperature and humidity jumps are characterized with several indices. Timing of the raco events is simply characterized by their initial and ending hours, whose histograms are shown in Fig. 5a. The beginnings of the events are rather uniformly distributed along the nighttime hours, with very few starting around midday and in the afternoon between hours 1100 and 1800 LT. In contrast, ending hours are conspicuously concentrated between 0900 and 1300 LT. This ending hour distribution suggests that the daytime warming of the valley is generally very effective in suppressing raco winds at La Obra. Indeed, as mentioned earlier, the daytime wind in the valley has a direction opposite to the raco. On the other hand, the fact that the onset time of raco winds shows absolutely no preference for any nocturnal hour suggests that their triggering mechanism may be of a synoptic or mesoscale nature as opposed to being controlled by the regular diurnal cycle of warming and cooling to be expected in a subtropical valley. In the CWH2013 case, for example, the valley exit jet begins typically within 1–3 h after sunset. Figure 5b describes the temperature jumps observed at the beginning of raco events. These jumps are defined as the temperature at the first hour of the raco event minus the minimum temperature of the three hours prior to the beginning of the event. This hour range is considered because the total temperature jump is not always fully developed in the exact hour in which VRACO surpasses the $4\,m\,s^{-1}$ threshold. The figure shows that temperature jumps are rather uniformly distributed between 0° and 10°C, with one extreme value reaching over 15°C. As stated before, these sudden nocturnal warmings are quite noteworthy as they occur during cold nights. Ending temperature falls (not shown) are less prominent than the initial rises. For the few events that end during the night, the ending temperature drops are 0°–5°C, but since most of the events finish during the morning any potential cooling at the end of the raco event is counteracted by the daytime warming, resulting in a typical warming at the end of the event by 0° to 3°C. Analogous results are found for water vapor mixing ratio jumps (not shown): beginning jumps show a uniform distribution between 0 and $3\,g\,kg^{-1}$ of drying, with maximum values of $5\,g\,kg^{-1}$, while at the end of the events a moistening between 0 and $3\,g\,kg^{-1}$ is generally observed. Figure 6a shows the association between the jumps in temperature and the drops in water vapor mixing ratio at the beginning of raco events. A negative correlation is observed ($r \sim -0.57$) indicating that in general the larger the initial increase in temperature, the larger the drop in mixing ratio. This association suggests that raco air parcels descend from higher altitudes, with the drier and (potentially) warmer

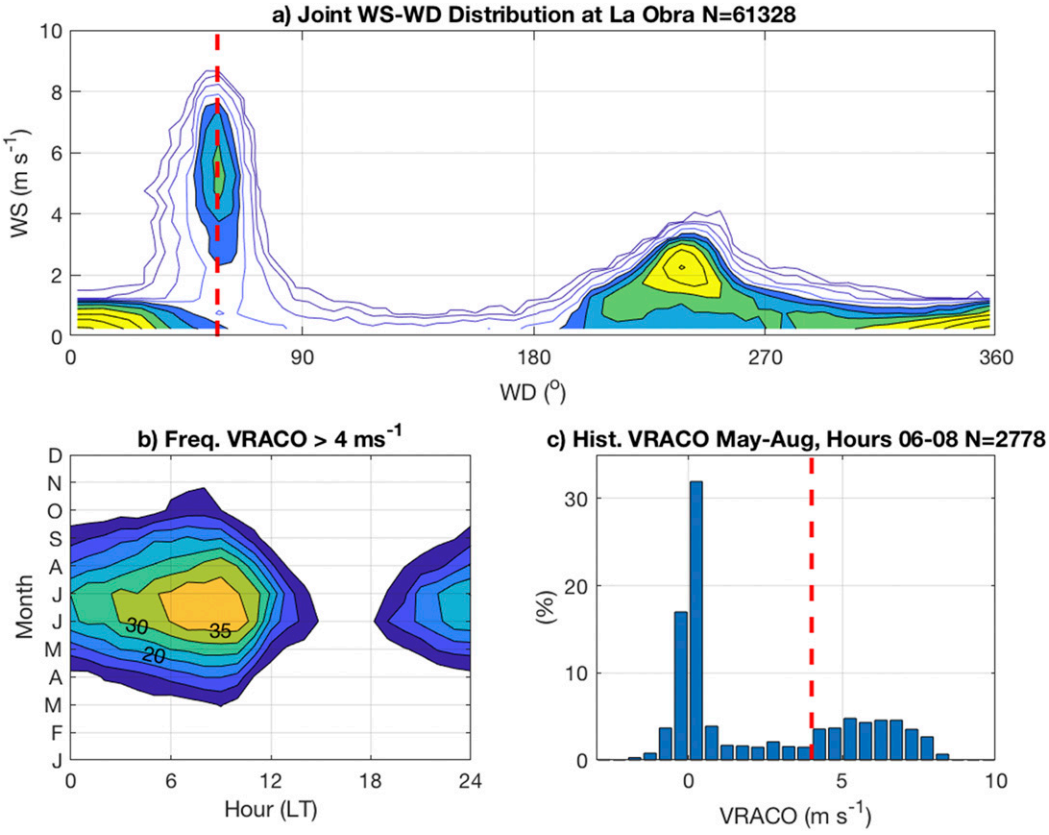

FIG. 4. (a) Joint frequency distribution of hourly wind speed and wind direction at La Obra for the full data record (total number of hours: 61 328). Frequency contours nonlinearly spaced at 0.0025, 0.0063, 0.0159, 0.0400, 0.0634, 0.101, 0.159, 0.252, 0.400, 0.634, and 1.00 [all values in % s $(m\,°)^{-1}$]. Red dashed line indicates raco wind direction of 57°. (b) Hourly and monthly distribution of the frequency (%) of wind speeds projected along 57° being larger than 4 m s^{-1}. (c) Frequency histogram of wind speeds projected along 57° for hours 0600–0800 LT during the months of May to August (total number of hours: 2778). Red dashed line marks the threshold of 4 m s^{-1} used to define raco hours.

parcels coming from higher elevations. Finally, intensity and duration indices are shown in Fig. 6b. The former is simply defined as the maximum VRACO during the event and the latter by the number of hours it comprises. Most raco events last less than 18 h, although there are a few with durations from one up to almost three days. In the shorter range of durations, a positive correlation between intensity and duration is found, but the maximum hourly averaged intensity appears to be limited to around 8 m s^{-1}. Nevertheless, instantaneous gusts up to 17 m s^{-1} have been measured at this site. No correlation is observed between raco intensity and initial temperature or water vapor mixing ratio jumps (not shown).

As seen in Fig. 2, raco events tend to cluster in groups of several consecutive days, followed by nonraco periods of comparable length. This is evaluated by characterizing each day according to the number of raco hours occurring between 0100 and 1200 LT. Four classes of days have been defined according to this number: 1) 0 raco hours, 2) 1–4 raco hours, 3) 5–8 raco hours, and 4) 9–12 raco hours in the 0100–1200 LT period of each day. Figure 7a shows the frequency distribution of these classes for the seven years with full May–August records. Only about half of the days in the May–August period show no raco hours during the night, while about 25% of the days have raco during almost all of the night. These results confirm that raco hours are quite frequent at this site during winter. We finally define a raco episode as a group of consecutive days having 5–12 raco hours in the 0100–1200 LT period. A total of 158 episodes are detected in the observational period, resulting in an average of 5–6 episodes per month. Figure 7b shows the distribution of the duration of raco episodes, which can last for up to seven days, although about 75% of the episodes are only one or two days long. These results are generally consistent with those of RG2004, who found a return period for raco episodes of about one per week and a typical duration of 1–2 days, but we

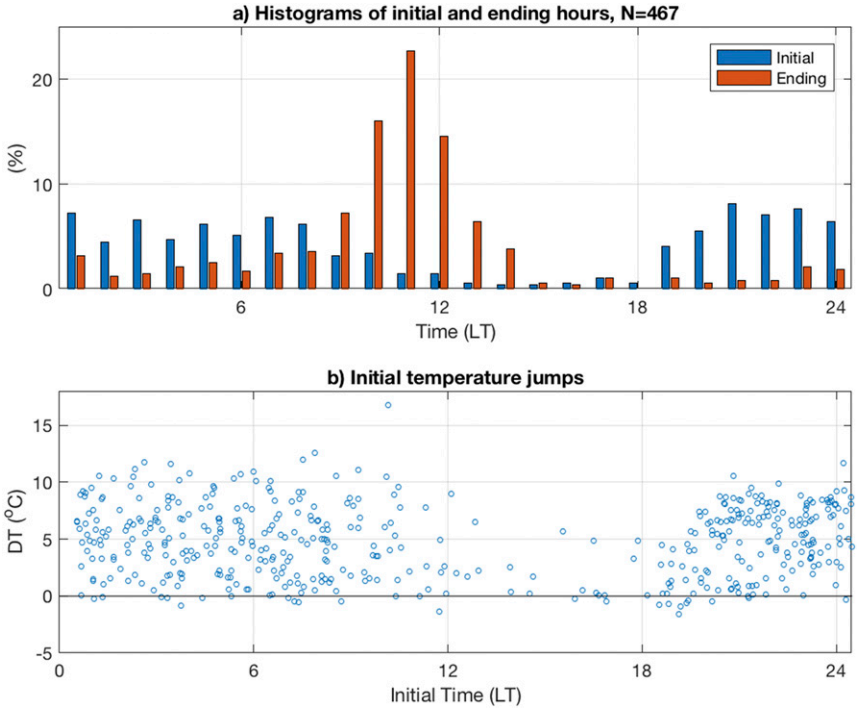

FIG. 5. (a) Frequency distributions of initial (blue) and ending (red) hours of raco events during the months of May to August (total number of events: 467). (b) Hourly distribution of temperature jumps associated with the beginning of a raco event. A uniformly distributed random number between −0.5 and 0.5 was added to the initial hour of each event in order to better visualize the variability.

stress here that individual raco hours at La Obra are quite frequent during winter showing up in 50% of the days between May and August, a frequency that, as pointed out previously, could be even larger if a lower VRACO threshold had been used to define them.

b. *Association of raco winds at different locations and with other variables*

The association of raco winds at La Obra with winds at other sites in the vicinity is explored in Fig. 8. Figure 8a shows the scatter of VRACO at La Obra with VRACO at Almenar, located about 3 km to the west of La Obra, just downwind of the canyon exit toward the Santiago Valley and about 110 m below the altitude of La Obra. Since the Almenar station was installed only at the end of 2017, the comparison is made just for the May–August nights of 2018. The figure shows that raco is more frequent at La Obra than at Almenar. Considering all the hours in which VRACO at La Obra surpasses $4\,m\,s^{-1}$, in only about 35% of them the value of VRACO at Almenar surpasses $2\,m\,s^{-1}$. The intensity of raco at Almenar is also less than at La Obra, the different heights above ground level of each sensor notwithstanding. Figure 8b, on the other hand, explores the association of VRACO at La Obra and VRACO at El Manzano located about 9 km east from La Obra, inside the Maipo Canyon, and at an altitude about 100 m higher than La Obra. In this case, the comparison is performed for nocturnal hours of May–August in the 2001–04 period in which both stations operated simultaneously. Figure 8b suggests that periods with intensified VRACO at La Obra have also intensified down-valley winds at El Manzano. The intensities at both sites are similar, but they are not directly comparable because of the different measuring heights above the ground (4 m at La Obra and 10 m at El Manzano). The onset of raco episodes at El Manzano is less marked than at La Obra, showing a more gradual increase in winds and smaller jumps in temperature and humidity (see Fig. 10 in section 4).

Another covariability of interest is that of raco winds and the pressure field. The pressure gradient along the canyon is characterized with pressure observations at La Obra and Guayacán, a station located about 12 km inside the Maipo Canyon (see Fig. 1). To eliminate the effect of the different altitudes of both stations, the analysis is based on anomalies of their pressures with respect to their corresponding overall mean value. The relationship between VRACO at La Obra and the difference of pressure anomalies at Guayacán minus La

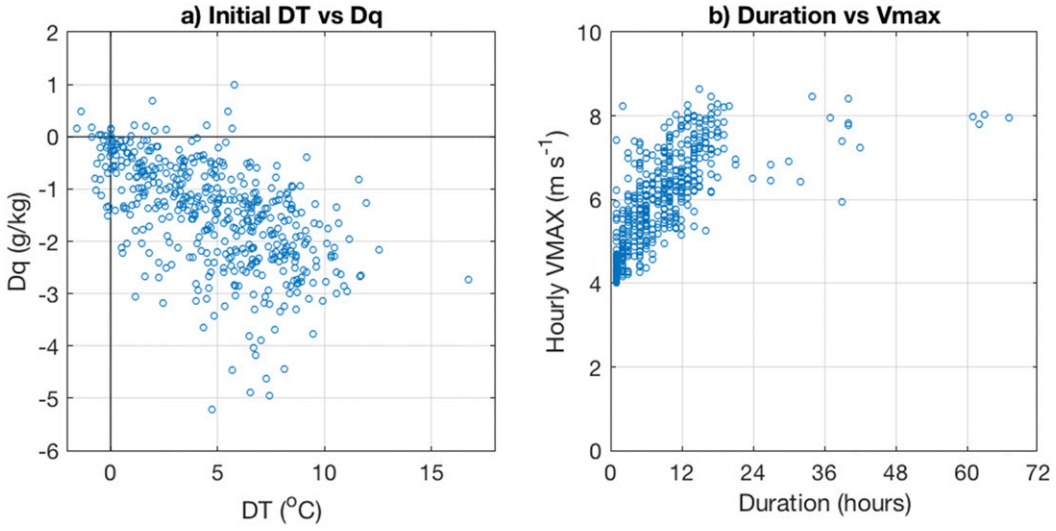

FIG. 6. (a) Relationship between jumps in temperature and water vapor mixing ratio associated with the beginning of raco events in the period from May to August. (b) Relationship between maximum hourly wind speed during each event, as projected along the raco wind direction, and the duration of the raco event for the period from May to August.

Obra is shown in Fig. 9a, for nighttime hours of May to August. Two rather separated point clouds appear in this figure. When the pressure anomaly difference is smaller than about 1 hPa, VRACO is small, but when that value exceeds +1 hPa, VRACO increases to above $4\,m\,s^{-1}$ and a direct relationship between pressure gradient and raco intensity is observed. The highest VRACO values of about $8\,m\,s^{-1}$ are obtained with pressure anomaly differences of up to 3 hPa, which are quite significant given the relatively small horizontal distance between the stations. Moreover, the strong association between VRACO and pressure gradient highlights the nongeostrophic character of the raco wind. In terms of the relationship between VRACO and the synoptic variation of the pressure field, there is a tendency to observe raco events during periods in which surface atmospheric pressure is decreasing. This is evaluated in Fig. 9b by showing histograms of hourly

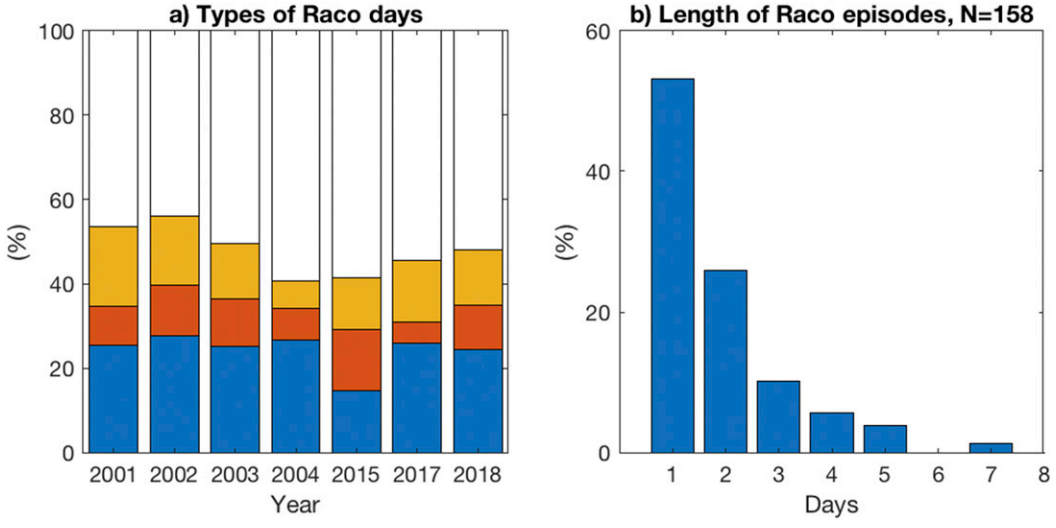

FIG. 7. (a) Percentage of days in the May–August period having days with 0 (white), 1–4 (yellow), 5–8 (red), and 9–12 (blue) raco hours in the period between 0100 and 1200 LT of each day. (b) Frequency histogram of the length of raco episodes defined as successive days having 5–12 raco hours in the period between 0100 and 1200 LT of each day. Years 2005 and 2016 of the database have not been considered because of missing data.

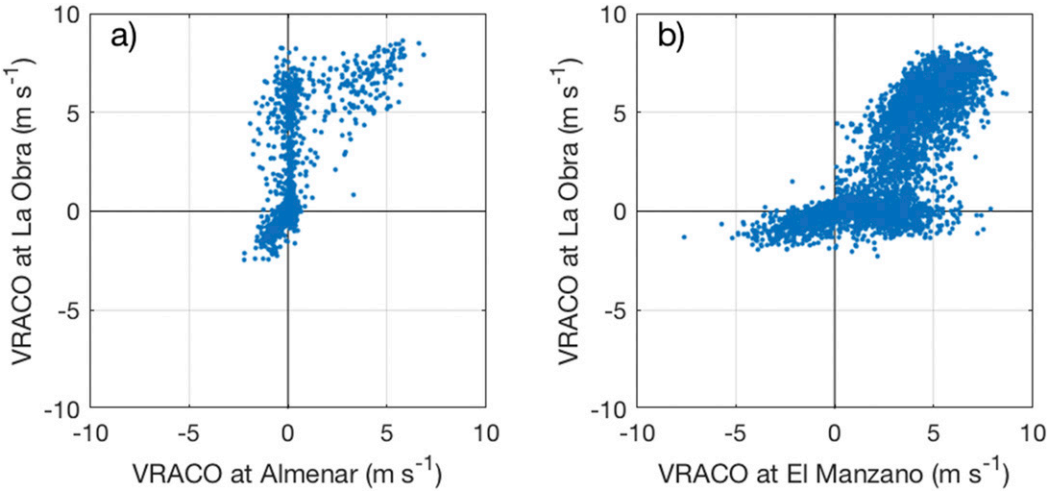

FIG. 8. (a) Scatterplot between La Obra wind speeds projected along the raco wind direction (57°) and the same but for Almenar station. Only hours between 0100 and 1200 LT and months from May to August of 2018 are considered. (b) Scatterplot between La Obra wind speeds projected along the raco wind direction and the same but for El Manzano station. The raco wind direction for El Manzano is 90°. Only hours between 0100 and 1200 LT and months from May to August of 2001–04 are considered.

pressure changes at La Obra. Before computing the pressure changes, however, a 25-h moving-average filter has been applied in order to smooth out the diurnal and semidiurnal cycles of atmospheric pressure at the site and keeping only the synoptic variability in the time series. Furthermore, the nocturnal hours from May to August have been separated between raco and nonraco hours as described before. As must be, the global histogram of hourly pressure changes is quite symmetric with respect to zero. Pressure changes during raco hours, however, are clearly biased toward negative pressure changes, and the more intense the pressure drop, the larger the conditional probability of having raco wind at La Obra. This points to the preference for raco winds to occur during the development of coastal lows (e.g., Garreaud et al. 2002) or the approach of synoptic low pressure systems, as was also found by RG2004. Moreover, the weaker synoptic variability during summer makes the observed range of hourly pressure changes more restricted than during winter

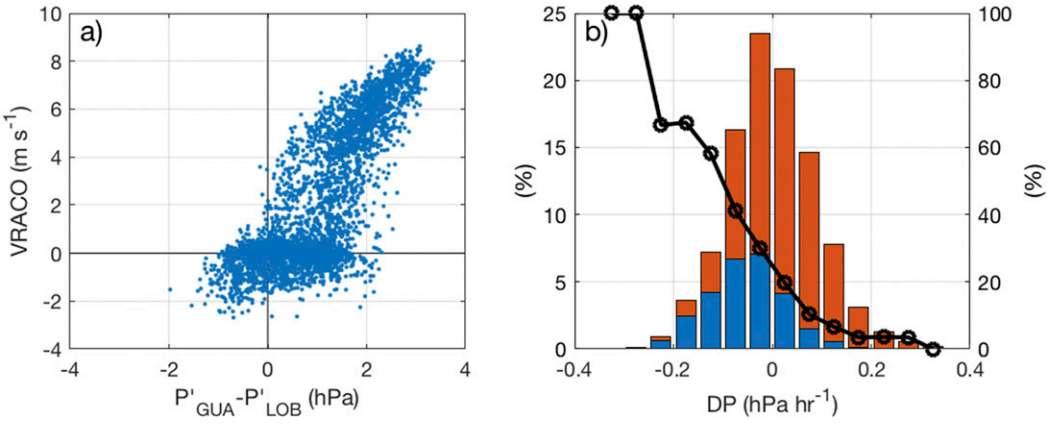

FIG. 9. (a) Scatterplot between La Obra hourly wind speeds projected along the raco wind direction and the pressure anomaly differences between Guayacán (GUA) and La Obra (LOB) stations. Only hours between 0100 and 1200 LT and months from May to August are considered (years 2015–18). (b) Frequency histogram (left scale) of hourly pressure changes at La Obra for raco (blue) and nonraco (red) hours in the months from May to August and hours 0100–1200. The pressure time series has been smoothed with a centered 25-h moving average before computing hourly changes. Black line indicates the fraction of raco hours for each class of pressure change (right scale).

(not shown), which could be related to the near absence of raco events during the warm period of the year.

Regarding the association between raco and cloudiness, the solar radiation measurements at La Obra allow for a preliminary analysis. To do so, we compute the sum of solar radiation received at the station over the morning hours between 0700 and 1200 LT of each day in the May–August period. That sum divided by the corresponding value for a clear day is used as a proxy for a clear-sky index, and 1 minus the latter defines a cloudiness index. We consider the histogram of this index over all days that have VRACO $> 4\,\mathrm{m\,s^{-1}}$ in at least 4 of the 6 h between 0700 and 1200 LT. In about 80% of the resulting cases, the cloudiness index is less than 0.2, confirming that raco episodes typically occur under clear-sky conditions. However, about 10% of cases have cloudiness index greater than 0.5, which point to raco episodes under cloudy skies. Whether these two types of raco episodes match the two different synoptic patterns described by RG2004 deserves further study, but the fact that raco winds can also occur during cloudy conditions suggests that radiative cooling of the canyon air mass is not always needed for the phenomenon to be observed.

4. Special observations

Synoptic-scale weather conditions during the 22–26 July 2018 IOP were characterized at the 500 hPa level by an incipient cutoff low (COL; e.g., Fuenzalida et al. 2005) on 23 July [Fig. D(a) in the online supplemental material], that develops centered at about 35°S as strong ridging progresses south of this area. The COL develops over the coast between dawn and early morning of 24 July, drifting steadily eastward thereafter (not shown). A strong westerly flow dominates the mid- and upper troposphere over central Chile on 23 July, according to the Santo Domingo radiosonde [Fig. D(e)]. This condition ends late on 25 July when a new trough heads toward central Chile [Fig. D(b)]. Near-surface (1000 hPa level) weather chart depicts a type A coastal low (e.g., Garreaud et al. 2002; their Fig. 6a) for 23 July [Fig. D(c)] that deepens as the cold anticyclone drifts eastward. Low coastal surface pressure deepens again on 25 July [Fig. D(d)] as the trough-associated frontal depression approaches the continent, shaping now a type B coastal low (Garreaud et al. 2002; their Fig. 6b). Here, the Santo Domingo radiosonde [Fig. D(f)] looks similar to the one depicted in Fig. D(e) in terms of the strong warming/drying of the lower troposphere and strong westerlies aloft. However, middle to high clouds complete the characterization of these type B coastal lows. These synoptic weather conditions do not differ substantially from the conditions described by RG2004, although COLs can modulate their intensity and duration.

Surface observations of wind, temperature, and water vapor mixing ratio at La Obra for an eight-day period including the IOP were shown in Fig. 2. Corresponding time series for stations Almenar and El Manzano are presented in Fig. 10. While raco events were observed at La Obra every day from 23 to 26 July (Fig. 2a), the phenomenon was less frequent at Almenar and El Manzano (Fig. 10a), where it was even absent at both sites in the night of 24 July. Temperature and humidity values also show marked jumps associated with raco winds at Almenar, but they are not as apparent at El Manzano. The changes of wind and temperature vertical profiles caused by a raco event are illustrated in Fig. 11 for that occurring at Almenar between 0000 and 0600 LT 25 July. Before the raco event (0000 LT), the zonal wind profile at Almenar shows a well-defined maximum ($\sim 10\,\mathrm{m\,s^{-1}}$) of easterly flow at about 1500 m MSL ($\sim$700 m AGL) and a surface-based inversion in the temperature profile. The profiles at El Manzano, on the other hand, show a deeper and more complex-structured layer of easterly flow and a less marked surface inversion. During raco conditions at Almenar (0600 LT), the level of maximum easterly flow descends about 500 m, the maximum wind speed increases up to almost $15\,\mathrm{m\,s^{-1}}$ and surface winds vary between 5 and $10\,\mathrm{m\,s^{-1}}$. Concurrently, the layer below 1200 m MSL ($\sim$400 m AGL) over Almenar experiences a significant warming of around 5°C, whereas near the ground temperatures increase up to 12°C due to the dissipation of the surface inversion that existed at 0000 LT. Changes of the zonal wind and temperature at El Manzano are much less dramatic as compared to those over Almenar.

a. *Radiosondes*

The complete evolution of the vertical structure of wind and temperature profiles during the IOP can be observed in Figs. 12 and 13 based on the radiosondes at Almenar and El Manzano. A jetlike structure of the zonal wind (along the valley axis) is quite prominent at Almenar (Fig. 12a), with maximum speeds of up to $12\,\mathrm{m\,s^{-1}}$ at about 1500 m MSL or 700 m AGL, contrasting to the $\sim 30\,\mathrm{m\,s^{-1}}$ and 100 m AGL height of the CWH2013 valley exit jet. The easterly jet in Fig. 12 has a diurnal modulation: the jet weakens during the afternoon of some days. It also features a vertical displacement, touching the surface for some hours at the dawn of 23 July and for most of the night of 25 July. These periods coincide with the raco observations at the surface shown in Fig. 10a. The low-level easterly flow is confined below 2500 m MSL, with westerly components dominating aloft as also described by RG2004. Just about 10 km inside the Canyon to the east, the zonal flow over El Manzano (Fig. 12b) shows a strikingly different

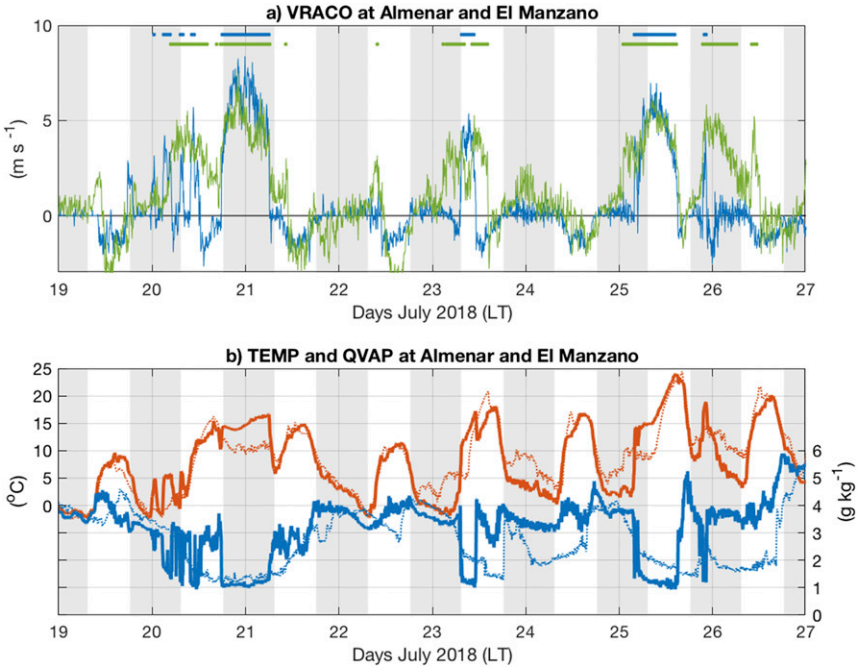

FIG. 10. (a) As in Fig. 2a, but for stations Almenar (blue) and El Manzano (green). (b) As in Figs. 2b and 2c, but for stations Almenar (continuous bold) and El Manzano (dotted fine). Temperature (water vapor mixing ratio) shown in red (blue) at the left (right) scale. The RACO2018 IOP extended from noon 22 to noon 26 Jul 2018. Solid lines at the top of (a) mark raco conditions as defined for each station with a threshold of 3 m s^{-1}.

structure. The layer with easterly wind here is present through a deeper height range up to about 3000 m MSL but its intensity is weaker and has no well-defined jet maximum as compared to the Almenar profiles. With weaker easterlies, the diurnal modulation over this site appears more marked than over Almenar. With respect to the meridional wind component, the easterly jet layer at Almenar is accompanied by a weak northerly component (Fig. 12c) while at El Manzano a weak southerly component prevails (Fig. 12d). These meridional components are probably driven by the local orientation of the canyon at each site (Fig. 1b). Above the layer of easterly flow, strong north-northwest winds also with a jetlike structure (i.e., up to 16 m s^{-1} below 4000 m over Almenar) are observed and are most readily interpreted as barrier winds resulting from the blocking of the westerly upper airflow by the Andes (e.g., section 3 in RG2004 and references therein).

The evolution of the vertical structure of potential temperature and water vapor mixing ratio is shown in Fig. 13. A two-layer structure in the vertical is apparent, loosely defined by the white contours in Fig. 13. The bottom layer is relatively cold and humid compared to the upper layer. While the former has large synoptic variability in terms of height, the latter displays significant temporal changes in temperature and humidity. As shown by the red isotachs, the easterly flow at Almenar resides in the upper warmer and drier layer, especially in the region with significant stability atop the cold and humid bottom layer. Raco events at the surface are associated with the upper warm and dry layer reaching down to the surface, which is especially clear in the humidity plots (Figs. 13c,d). The warming and drying, however, is experienced not only by the near-surface air but throughout the lower troposphere, a sign of possible regional forced subsidence as discussed in the context of coastal lows by Garreaud and Rutllant (2003).

Figure 14a shows the time–height evolution of the pressure difference between El Manzano and Almenar together with bottom marks indicating the occurrence of surface raco conditions at El Manzano, La Obra, and Almenar, and a reference red contour delimiting the −4 m s^{-1} isotach of zonal wind at Almenar. Figure 14b shows surface pressure anomalies at Guayacán and La Obra for the same period. As was described for the climatology, the raco wind at the surface closely follows the in-valley pressure gradient, occurring when the pressure anomaly at Guayacán is larger than at La Obra (Fig. 14b). This surface pressure signal is consistent with the pressure gradient aloft as shown by Fig. 14a, at least up to about 1000 m above the ground, coinciding with the region of enhanced easterly flow at Almenar (red dashed contours). In contrast

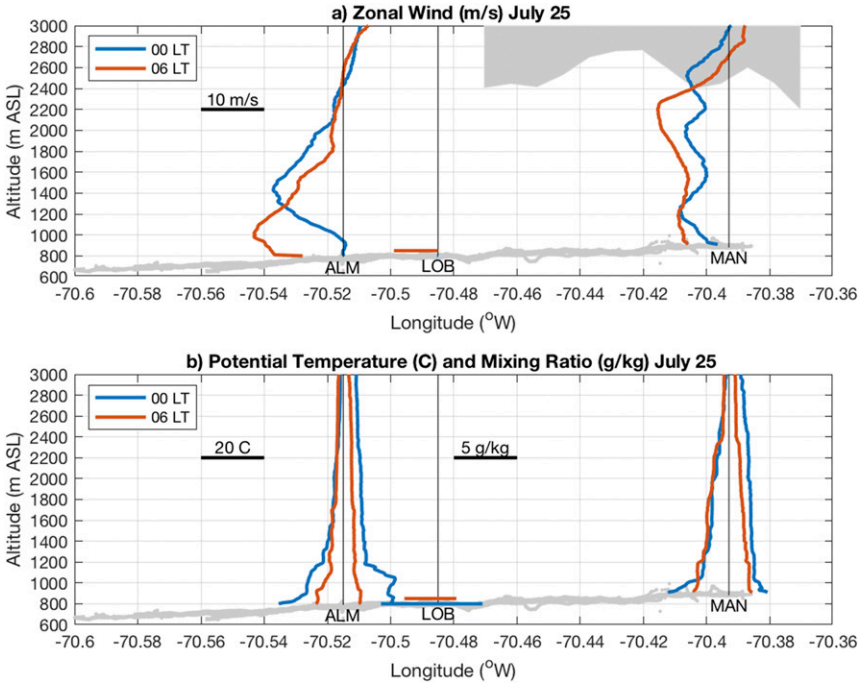

FIG. 11. Vertical profiles before (0000 LT, blue) and during (0600 LT, red) raco conditions at Almenar for the night of 25 Jul 2018. (a) Zonal wind speed profiles over Almenar (ALM) and El Manzano (MAN). Vertical lines over each site mark the value of 0 m s^{-1} and the wind speed scaling is provided at 2200 m MSL. (b) As in (a), but for potential temperature (reference value of 30°C at the vertical line) and water vapor mixing ratio (reference value of 0 g kg^{-1} at the vertical line). In all cases, surface values at La Obra (LOB) are shown with the same scalings and color codes. The gray dots at the bottom show the altitude of the road along the canyon, which is approximately at its bottom. The shaded region at the top of (a) represents the variation of the area of meridional cross sections along the canyoń exit corridor below 2000 m MSL (arbitrary units).

to the CWH2013 case, in which the along-canyon pressure difference responded to a cooling of the air mass inside the canyon, the pressure difference in the raco case responds mainly to the warming at the exit of the canyon, as illustrated by Fig. 11b.

b. Sodar

A finer-grain picture of the evolution of the vertical profile of wind over Almenar is provided by the sodar (Fig. 15). Unfortunately, due to measurement constraints with the sodar, the data do not extend vertically beyond the level of maximum speed, so that it characterizes mainly the layer below the easterly jet described with radiosondes in Fig. 12a. Nonetheless, Fig. 15a illustrates well the dramatic changes of the zonal wind vertical profile over this site. Consistent with the radiosondes, the sodar suggests the existence of an easterly flow above 400 m AGL for most of the period. The raco events at Almenar constitute a surface manifestation of a rapid descent and intensification of this easterly flow that in a couple of hours drops from about 700 m AGL to the surface (days 23 and 25). Interestingly, at the end of 25 July there is a brief raco event at the surface that is observed by the sodar but completely overlooked by the poorer-temporal-resolution radiosondes. The strength of the easterly flow aloft may be a factor on the occurrence, intensity, and duration of the raco wind at the surface, as the largest magnitudes of the (negative) zonal wind are generally observed when the easterly jet moves down toward the surface. The sodar-derived profiles of vertical velocity (Fig. 15b), on the other hand, show a tendency for negative values (subsidence) in the region below the easterly flow, with magnitudes that can be up to 2 m s^{-1}, similar to those reported by CWH2013 for the Weber Canyon valley exit jet. These are very large values that support the hypothesis that the dry and warm raco air parcels have been forced to descend by a strong interaction between the flow and the topography.

c. Mobile ceilometer

In the July 2018 IOP a Vaisala CL31 ceilometer was mounted in the back of a pickup truck in order to

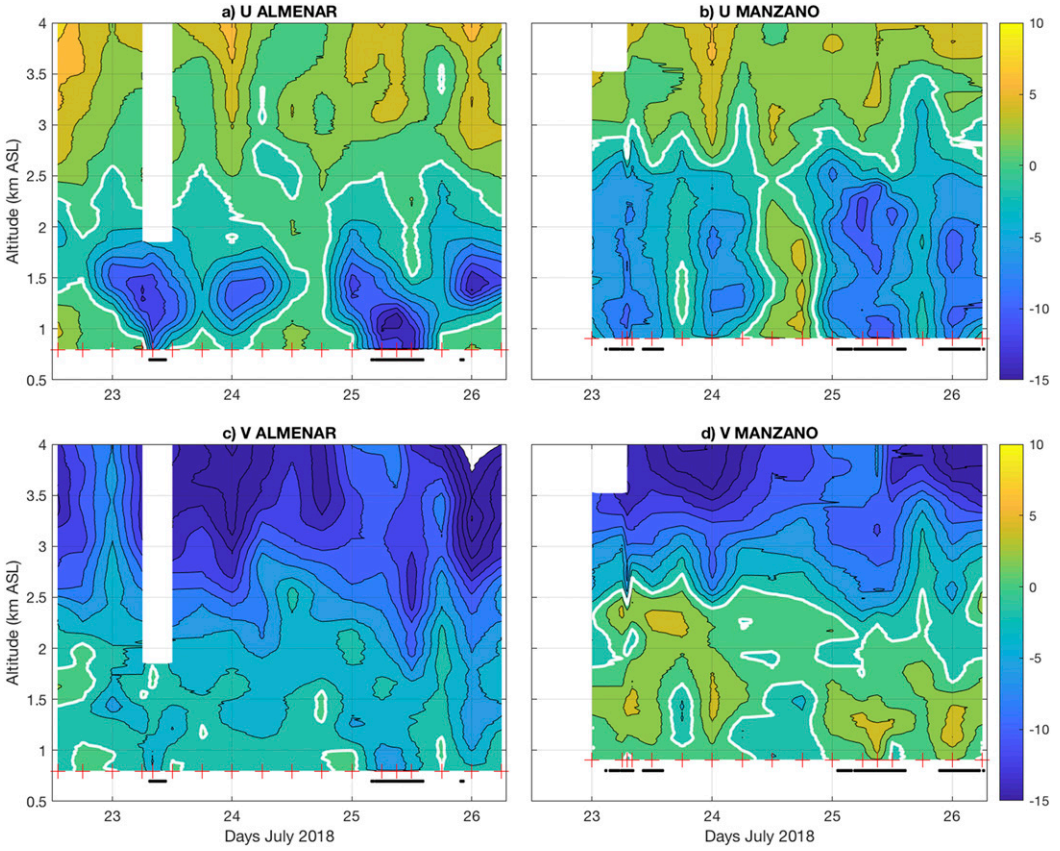

FIG. 12. (a) Time–height cross section of zonal wind at Almenar obtained with radiosondes launched at the times marked with a red cross at the bottom of the figure. Contours every 2 m s^{-1}. Blue (green) colors indicate negative (positive) values and white contour marks the 0 m s^{-1} value. (b) As in (a), but for El Manzano station. (c) As in (a), but for the meridional wind component. (d) As in (c), but for El Manzano station. In all panels, solid lines at the bottom mark the occurrence of surface raco conditions as described in Fig. 10.

describe the variation along the canyon of the near-surface aerosol layer during raco events. Concurrently, an iMet-XQ sensor was installed on the truck roof to measure instantaneous temperature, relative humidity, pressure, and GPS position along the path followed. While stationary ceilometers have been for some time successfully used in Santiago and elsewhere to characterize the vertical structure of aerosols in the planetary boundary layer (PBL) with high temporal and vertical resolution (Muñoz and Undurraga 2010; Caicedo et al. 2017), the application of a mobile ceilometer to characterize the horizontal variability of aerosol layers in the PBL is rather new with only few reports in the literature (Peng et al. 2017). Figures 16 and 17 provide two examples of the measurements with the mobile system. Figure 16 shows a down-valley transect from El Manzano to the canyon exit performed between 0746 and 0814 LT 23 July 2018 with a length of about 18 km and an altitude drop of about 200 m between the initial and ending points (Fig. 16a). Figure 16b shows the time–height cross section of the backscatter intensity measured by the ceilometer along the route. Warm color regions are interpreted as aerosol-loaded air layers and blue regions as aerosol-free layers with low backscatter. Data near the surface below about 50 m AGL have been masked out because this instrument cannot fully measure backscatter very close to its telescope (Kotthaus et al. 2016). Also, intermittent peaks of backscatter along the transect are believed to correspond to tree branches above the street that momentarily block the laser ray as the truck passes below them. Figure 16b shows a strong contrast in the aerosol content of the near-surface atmospheric layer between the western and eastern portions of the transect, with the transition being located around Almenar at the time of measurement. To the west of this station, in the canyon exit region toward Santiago Valley, a higher aerosol load is observed in a layer whose top goes from about 100 m AGL near Almenar up to about 400 m AGL at the western end of the transect. To the east, inside the

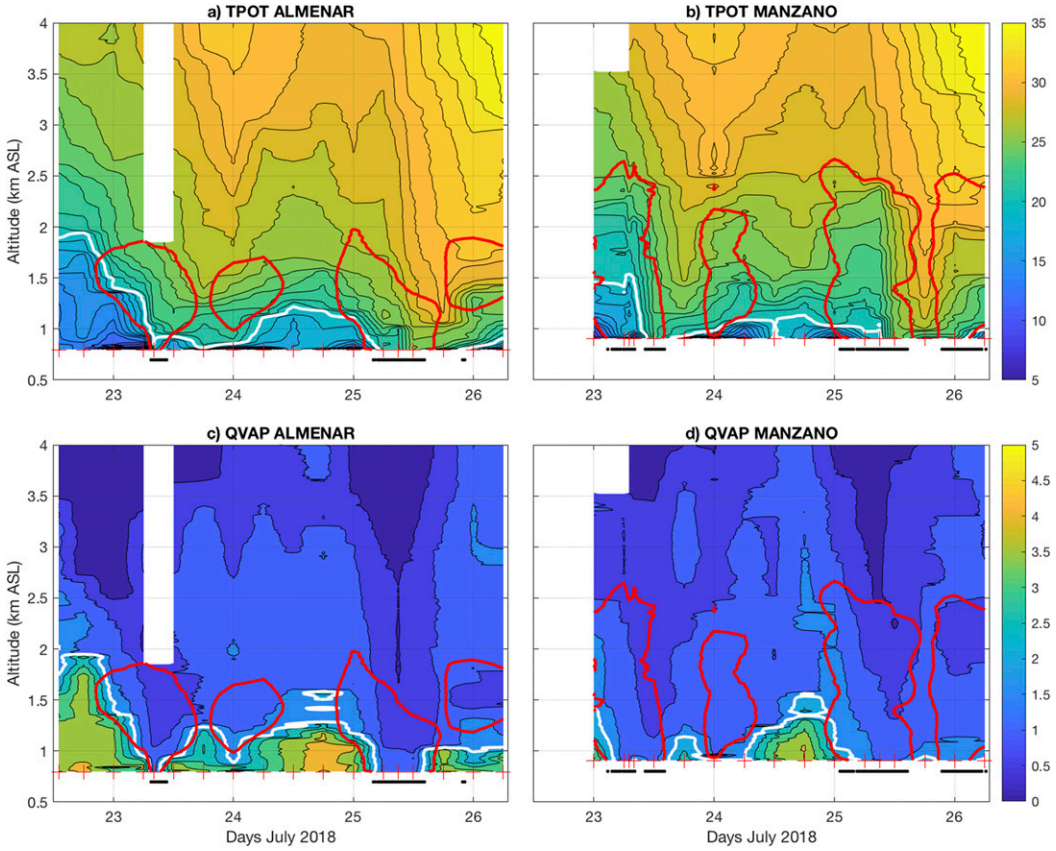

FIG. 13. (a) Time–height cross section of potential temperature at Almenar obtained with radiosondes launched at the times marked with a red cross at the bottom of the figure. Contours every 1°C. White contour marks the 20°C value. (b) As in (a), but for El Manzano station. (c) As in (a), but for water vapor mixing ratio, q. Contours every 0.5 g kg^{-1}. White contour marks the 2 g kg^{-1} value. (d) As in (c), but for El Manzano station. In all panels, solid lines at the bottom mark the occurrence of surface raco conditions as described in Fig. 10. In all panels the red contours mark the -4 m s^{-1} zonal wind isotach.

canyon, the air is relatively aerosol free. Concurrent measurements of near-surface potential temperature and water vapor mixing ratio along the transect are shown in Fig. 16c. Very sharp changes in temperature (~10°C) and humidity (~2 g kg^{-1}) are observed at the aerosol transition location in Fig. 16b. Based on the time labels and matching positions of the ceilometer, this temperature–humidity–aerosol front is located at this time about 500 m to the west of Almenar, leaving the station in its warm-dry-clean-windy side. In fact, on this day the Almenar station was under raco conditions between 0730 and 1030 LT (Fig. 10a). This front can be considered the limit between a cold pool residing to the west over the Santiago Valley and the warm, dry, and clean air associated with the raco wind to the east. At the front, the raco appears to separate from the surface and keep flowing westward atop the cold pool.

Interestingly, a similar front appears farther up in the valley near the El Manzano station. This second front is clearly noticeable in temperature and humidity discontinuities, but not as much in the aerosol signal, as both sides of the front appear to have relatively clean air. Time series at El Manzano for this day (Fig. 18) suggest that this second front passes over the station around 0930 LT. Before this time, potential temperature and mixing ratio are about 13°C and 2 g kg^{-1}, respectively, putting the station on the western side of the front according to Fig. 16c. Around 0930 LT, the mixing ratio drops rapidly to about 1.5 g kg^{-1} suggesting that the front has moved west and has left the El Manzano station on its eastern side. The temperature increases also rapidly at this time, with the frontal effect adding to the warming associated with the solar heating of the surface. While the wind speeds are similar before and after the frontal passage, wind direction shifts noticeably from east-southeast to north-northeast (Fig. 18a). Later in the day, around 1430 LT the up-valley flow reaches El Manzano producing a complete reversal in wind

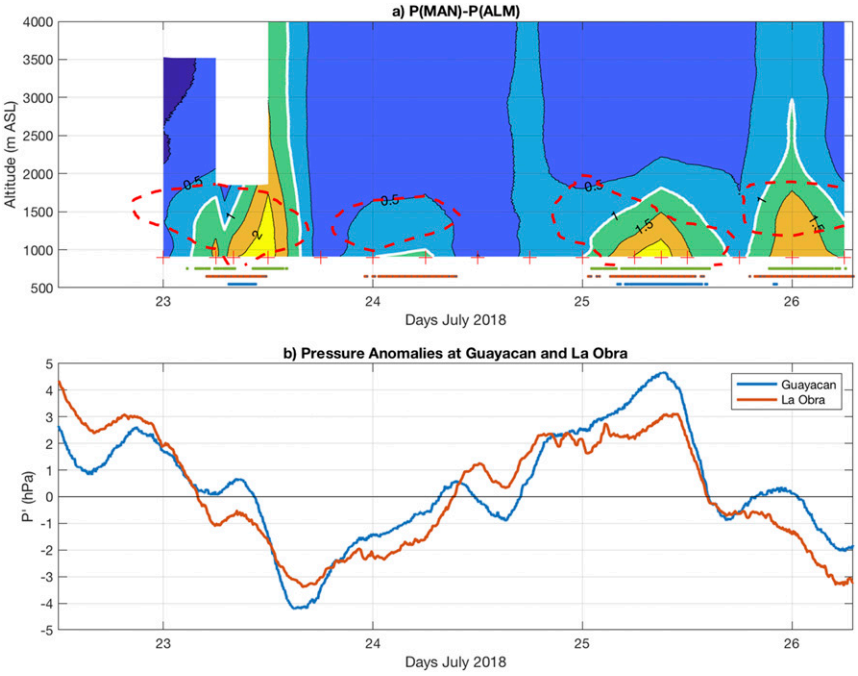

FIG. 14. (a) Time–height cross section of atmospheric pressure at El Manzano (MAN) minus pressure at Almenar (ALM) obtained with simultaneous radiosondes launched at the times marked with a red cross at the bottom of the figure. Contours every 0.5 hPa. White contour marks the 1 hPa value. Blue, red, and green solid lines at the bottom mark the occurrence of surface raco conditions at Almenar, La Obra, and El Manzano, respectively. (b) Time series of 5-min atmospheric pressure anomalies (with respect to the period average) at Guayacán (blue) and La Obra (red). In (a) the red dashed contours mark the $-4\,\mathrm{m\,s^{-1}}$ zonal wind isotach at Almenar.

direction, a sudden moistening and a slight cooling, marking the arrival of the more humid and potentially cooler valley air mass.

A couple of additional features are worth noticing in Fig. 16c. First, in the region between the two fronts at Almenar and El Manzano the surface potential temperature decreases significantly with altitude in the up-valley direction (by ~8°C) while water vapor mixing ratio increases (by $\sim 1\,\mathrm{g\,kg^{-1}}$). As these variables can be considered approximately conservative in this setting (nighttime subsaturated conditions), it follows that the truck is moving across trajectories of significantly different air parcels. Moreover, the potential cooling and moistening with ground altitude suggest that surface air parcels around Almenar are subsiding from higher altitudes than those near El Manzano, similar to what Fig. 1 of Mayr et al. (2018) suggests happens for air parcels impinging on the lee slope of a classical foehn flow downstream of a mountain barrier. Finally, a last curious feature of Fig. 16c is the contrasting spatial correlation between potential temperature and mixing ratio variability at each side of the Almenar front. To the west, in the cold pool air mass, there is a positive correlation between both variables, while the opposite occurs to the east. Positive correlations between temperature and water vapor mixing ratio are typically quoted in the literature for the atmospheric surface layer above sea and land (Platis et al. 2017 and references therein). Thus, the special condition in our measurements is the spatial anticorrelation between temperature and humidity observed on the eastern side of the raco front. Again, this pattern may be inherited from the general anticorrelation of potential temperature and water vapor content with altitude in a vertical profile, which may be imprinted on the surface transect as the truck successively probes parcels that have originated at various altitudes. As the temperature–humidity correlation has important practical and theoretical implications (Ward 2017; De Bruin et al. 1999), this problem may be investigated further in the future.

Twenty-nine transects with the mobile ceilometer system were performed during the nights and early mornings of 23–25 July 2018 (general time frame from 0630 LT until 1200 LT of each day; available as supplemental material). Like that of Fig. 16, the longest legs covered the route between El Manzano and the canyon

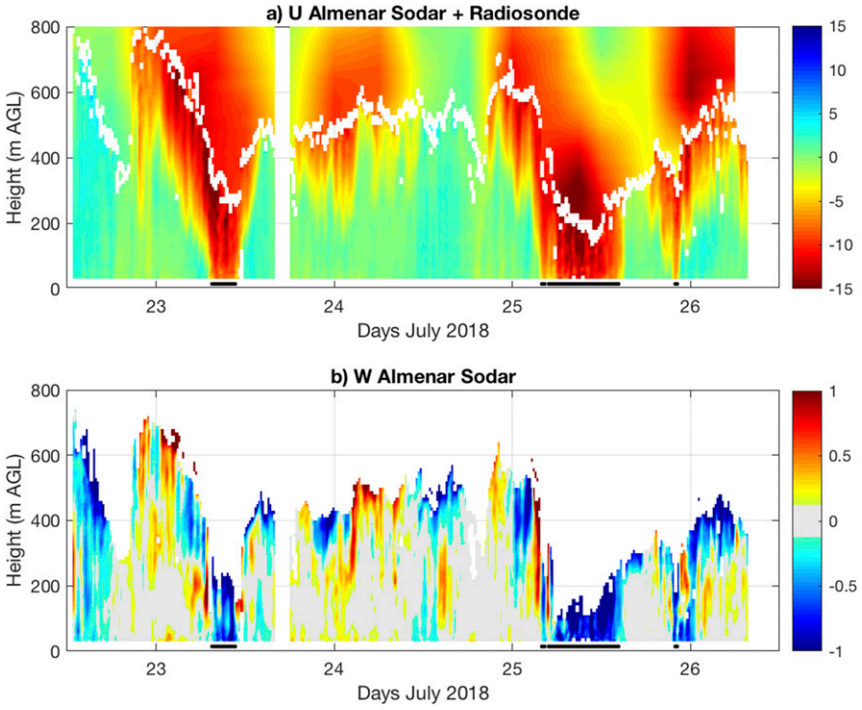

FIG. 15. (a) Time–height cross section of zonal wind ($m\,s^{-1}$) at Almenar measured by sodar. The upper portion of the field beyond the sodar data range (white zone) has been filled with interpolated radiosonde data. Black solid lines at the bottom mark the occurrence of raco conditions at the surface. (b) As in (a), but for vertical velocity ($m\,s^{-1}$). A gray mask for values between -0.25 and $+0.25\,m\,s^{-1}$ has been applied in order to emphasize regions with larger magnitudes in vertical velocity.

exit in about 30 min, although there were also shorter legs and static periods. Unfortunately, in 11 transects the iMet-XQ sensor malfunctioned, so that surface temperature and humidity measurements were not available. Nonetheless, most of the features observed in Fig. 16 appear also in the remaining transects: the existence of the Almenar and the El Manzano fronts in the early morning, the negative surface potential temperature gradient between Almenar and El Manzano, and the contrasting correlations between temperature and mixing ratio variability. As the morning hours evolve, the Almenar front appears to move inside the canyon, with the aerosol-loaded valley air mass reaching El Manzano on 24 July around 1130 LT but being unable to do so on 25 July (see the supplemental material). The jumps in temperature and humidity, though, become less sharp in the later morning hours, especially in the case of temperature. On occasions, some layering in the valley air mass is observed, as shown in Fig. 17. This shorter transect probed the region from Almenar toward the Santiago Valley. Two or three aerosol layers are apparent in this figure as well as some undulations atop them, which could indicate some instability in the shear region between the near-surface slow-moving cold pool layer and the upper layer in which the easterly jet resides.

5. Discussion

In this final section we explore how the raco climatology and variability presented in the previous sections match the physical mechanisms described in the introduction, by which the terrain affects near-surface winds, namely, the thermodynamic (e.g., katabatic and valley winds) and dynamic (e.g., foehn and gap winds) forcings. As shown by Figs. 11a, 12a, and 15a, the raco wind appears to be the surface impact of an easterly wind jet residing typically at around 1500 m MSL (~700 m AGL at the valley exit). At La Obra and Almenar stations, the raco onset is characterized by an abrupt increase of wind speed along a well-defined down-valley direction, accompanied by a simultaneous increase in temperature and drops in absolute humidity and aerosol content. These sudden changes in surface variables are reminiscent of what is observed at stations subject to foehn winds (Richner and Hächler 2013), and can be interpreted as the surface arrival of air parcels that have been forced to descend rapidly from aloft, bringing with

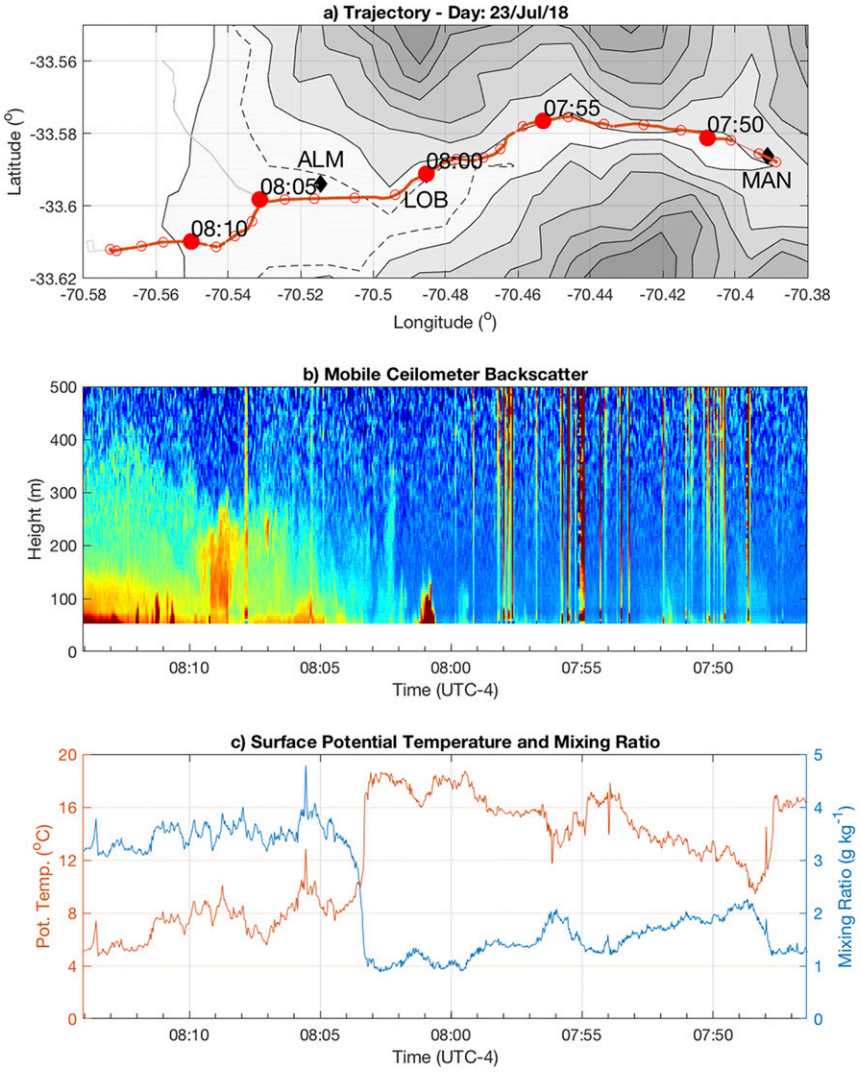

FIG. 16. (a) Maipo Canyon exit topography and route followed by the mobile ceilometer. Solid contours from 700 to 1900 m MSL every 200 m, dashed contour marks 800 m MSL. Red bold line marks the trajectory of the mobile ceilometer between 0746 and 0814 LT 23 Jul 2018. Red open circles are 1-min time marks, red solid circles are 5-min marks with time labels. Location of stations Almenar (ALM), La Obra (LOB), and El Manzano (MAN) are marked with solid black diamonds. (b) Time–height cross section of ceilometer backscattter (arbitrary scale) up to 500 m above the surface (backscatter values below 50 m AGL have been masked out due to an artifact of the instrument and vertical bands of high backscatter are the result of tree branches momentarily blocking the laser ray). (c) Time series of surface temperature (red, left scale) and water vapor mixing ratio (blue, right scale) measured concurrently with mobile ceilometer. The time scales in (b) and (c) are backward so that left and right sides correspond to panel (a).

them (potentially) warmer, dryer, and cleaner air. We shall reserve the name "raco" to refer to the strong winds at the surface and use the generic expression "upper jet" to refer to the easterly winds aloft. Accordingly, two main mechanistic questions can be addressed: 1) what is the forcing of the upper jet? 2) What forces this upper jet to eventually reach down to the surface and produce the raco?

Direct observations tell us little about the climatological characteristics (e.g., seasonal variability) of the upper easterly jet, as no long-term upper-air measurements exist in the Maipo Canyon. Its diurnal variation, however, was captured by observations during the IOPs showing that its intensity is greatest during the night and it weakens during daytime (Figs. 12a,b), more prominently

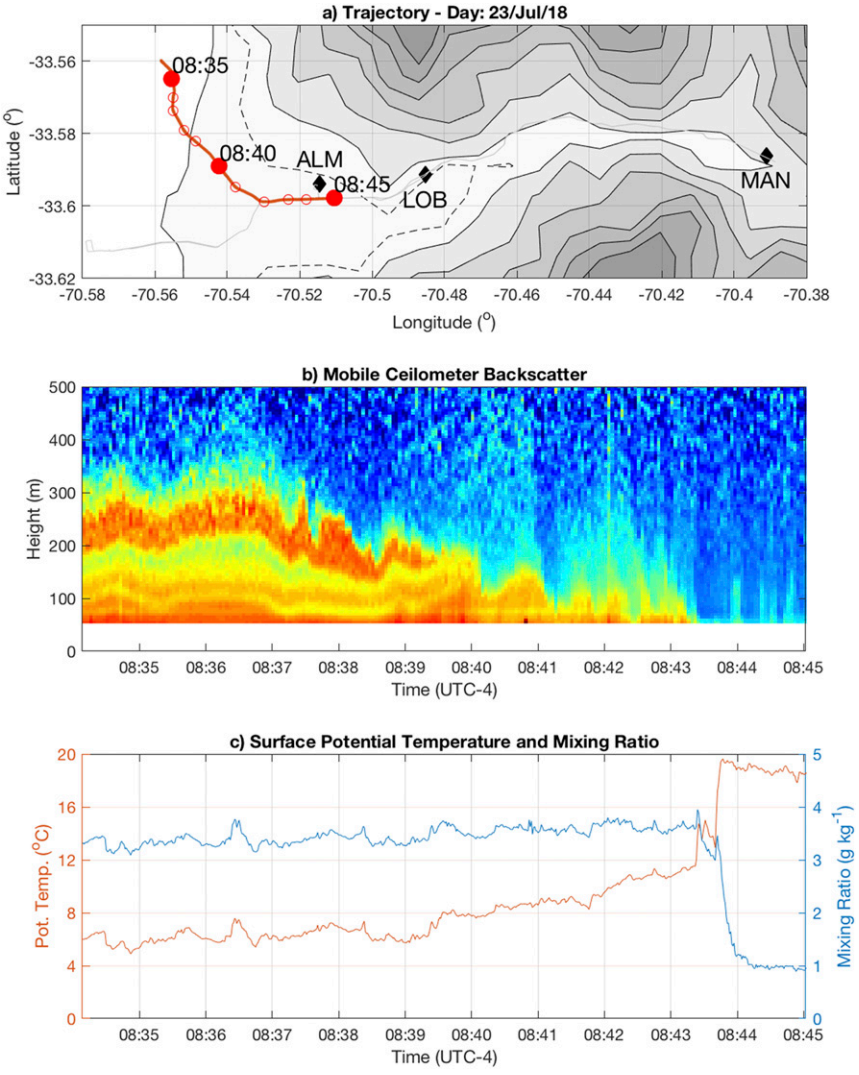

FIG. 17. As in Fig. 16, but for the mobile ceilometer transect in the period between 0834 and 0845 LT 23 Jul 2018.

so at El Manzano. The vertical extent and the structure of the zonal wind profile also differ between Almenar and El Manzano. At the exit of the canyon (Almenar) the upper jet has a well-defined nose-shaped profile with maximum speeds up to 12 m s^{-1} in a layer with easterly winds about 1000 m in depth. At Manzano, the easterly flow layer is about 1500 m deep and the wind profile has one or two maxima with speeds up to 10 m s^{-1}. The diurnal variation and the intensification of the jet at the canyon exit suggest that the valley exit jet mechanism may be operating in this case. An upper easterly jet at about 1500 m MSL (~700 m AGL) exiting from the Maipo Canyon has been reproduced by mesoscale numerical simulations of other events (Fig. 13 in Garreaud and Rutllant 2003; Castro 2018), suggesting that it is a feature common to all raco episodes. Moreover, the models produce similar jets emerging from the other neighboring valleys to the south and to the north of the Maipo Canyon. If the simulations are correct, then the upper jet is not a special feature of the Maipo Canyon, but it occurs in all similar valleys in the region, which is consistent with a thermodynamic mechanism like that of valley exit winds.

In contrast, the sudden surface impingement of the strong easterly flow appears to be highly localized, occurring mainly in the exit corridor of the Maipo Canyon, between La Obra and Manzano, and being both more frequent and stronger at the corridor exit than at the entrance. Stations deeper inside the Maipo Valley show only hints of raco conditions in traces of temperature and wind (not shown). With respect to their temporal variability, raco winds can start at La Obra

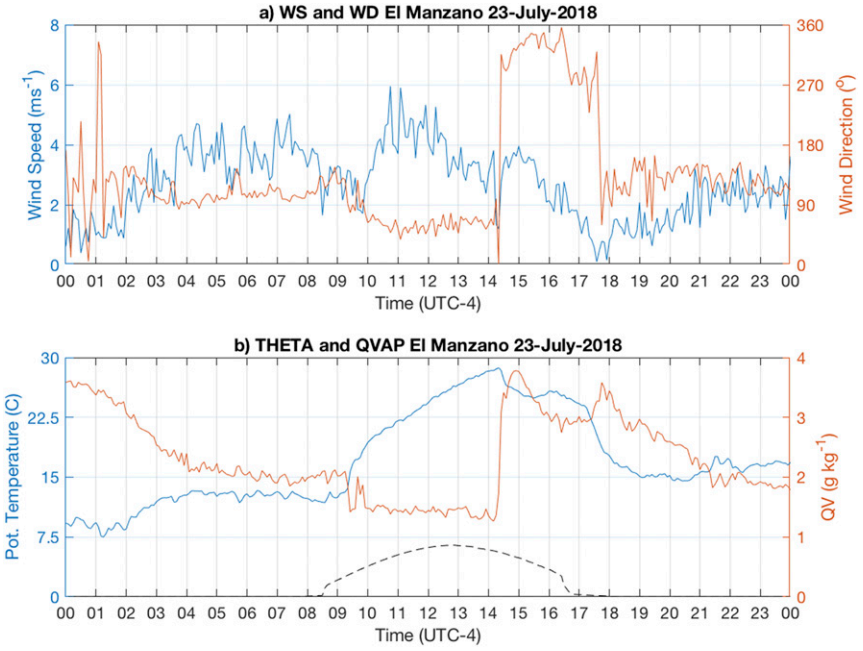

FIG. 18. (a) Time series of wind speed (blue, left scale) and wind direction (red, right scale) at El Manzano for 23 Jul 2018. (b) As in (a), but for potential temperature (blue, left scale) and water vapor mixing ratio (red, right scale). The black dashed line shows scaled solar radiation measured at La Obra in order to distinguish diurnal and nocturnal conditions.

indistinctively any time between 2100 and 0800 during the cold season (May–August) and they typically stop between 1000 and 1200 (Fig. 5a) when daytime up-valley winds develop. While their preference for nocturnal hours suggests a thermodynamic factor related to cooling or stability development in the valley, their sudden onset at any time during the night and the lack of any strong relationship between onset time and intensity put them at odds with purely thermodynamic mechanisms, which are usually repetitive and evolve continuously along the night. The same can be said with respect to their seasonal and synoptic variability. Thermodynamically forced nighttime valley winds are typically favored in summer conditions under weak synoptic forcing (Zardi and Whiteman 2013; CWH2013). On the contrary, the raco wind occurs almost solely in the cold season and has been associated with two well-defined synoptic patterns (RG2004), both characterized by rapid lowering of surface pressure to the west of the raco region (Fig. 9).

Based on the previous discussions, we hypothesize that a dynamic factor is playing a role at least in the second mechanistic question posed at the beginning of this section, namely, that of what forces the upper jet to descend to the surface producing the raco in the Maipo Canyon exit. Particularly appealing in this regard is the gap-wind mechanism, which has been proposed by Armi and Mayr (2007) to explain shallow-foehn cases along the Brenner Pass in the Alps. Based upon the hydraulic theory of stratified flow moving through a contraction (Wood 1968; Armi and Williams 1993), Armi and Mayr (2007) mention distinctive features that such flow may have in the downwind side of a gap: the development of a parabolic wind profile in a layer with a temperature inversion limited above and below by stagnant and more well-mixed layers. In the nomenclature of Armi and Williams (1993), this parabolic wind profile corresponds to ''structure 2'' of the possible solutions of the problem, but, depending on the forcing level, a ''structure 1'' solution is also possible, in which the maximum speed is at the surface. In the raco setting some of these features are indeed observed: the upper easterly jet often has a parabolic shape (see Fig. 11 and the complete set of vertical profiles in the supplemental material) and occurs in a stable layer between two more strongly mixed layers (Fig. 13a and supplemental material). The terrain constriction appears to be located within the exit corridor of the Maipo Canyon, where topographic contours (Fig. 16a) indicate a significant narrowing of the valley exit at 70.42°W, just about 6 km upstream of La Obra station. At this point, the transverse area below 2000 m MSL is only a third of the area immediately to the east and to the west (shaded region in Fig. 11a). This constriction may well be controlling the response of the down-valley flow, occasionally inducing the transition

to a fast supercritical descending flow on its downwind side toward the canyon exit. Alternatively, the level of the jet downwind of the constriction may be controlled by the dynamics of the cold pool existing at the bottom of the Santiago Valley and its intrusion into the Maipo Canyon, as illustrated by the ceilometer observations in Figs. 16 and 17, and those in the supplemental material. In both cases, the pressure gradient driving the outflow can result from the in-canyon pressure increase as the cool air draining down the Colorado and upper Maipo Valleys converges toward El Manzano or from the rapidly falling pressures to the west produced by the synoptic-scale setting (coastal low or approaching low pressure system). Thus, while the topographic constraint of the raco wind is fixed, several factors may play a role in its development (cold air pool properties, lower-tropospheric thermodynamic conditions, mesoscale pressure gradients, in-valley radiative cooling, etc.) providing for the significant observed variability in raco wind strength and associated temperature and humidity jumps.

6. Conclusions

We have presented a climatological characterization of the raco winds exiting the Maipo Canyon toward the Santiago Valley in central Chile, that complements and extends earlier work by RG2004. These episodic wintertime easterly winds begin abruptly at any time during the night at La Obra station, reach maximum hourly averages between 8 and 10 $m\,s^{-1}$ (with gusts up to 17 $m\,s^{-1}$) and terminate around noon with the onset of the up-valley westerly wind predominant during the afternoon. The sudden appearance of raco winds at the surface can be accompanied by a significant warming (up to 10°C) and drying (up to 3 $g\,kg^{-1}$). About half of the days in the period from May–August show at least one raco hour during the night, 25% of the days have more than six raco hours between 0100 and 1200 LT, and raco episodes last between 1 and 7 days with typical duration of 1–2 days. These findings are generally consistent with those reported previously by RG2004, but we have emphasized the sudden character of raco events and the abrupt changes in surface temperature and humidity associated with them. Furthermore, we documented the direct relationship between the intensity of raco winds and the along-canyon pressure gradient as well as the preference of raco events to occur during rapidly decreasing regional pressure patterns and clear skies, although still 10% of raco days are cloudy.

A 4-day observational campaign performed in July 2018 that included 6-hourly radiosondes launched from both extremes of the exit corridor of the Maipo Canyon, provided a more complete characterization of the vertical structure of a raco episode. A very marked upper easterly jet appears during the nights in the soundings at the exit of the corridor, at about 700 m AGL and with maximum intensity around 10 $m\,s^{-1}$. As shown by sodar measurements at the Almenar station, this jet descends rapidly on some occasions and impacts the surface as a raco event. Transects along the canyon performed with a mobile ceilometer and temperature and humidity sensors reveal that a frontlike feature exists between the cold pool at the bottom of the Santiago Valley to the west and the raco-affected conditions in the Maipo Canyon to the east. The very well-defined front shows significant changes of aerosol loads, temperature, humidity, and winds.

In the discussion section we examined how the aforementioned observations match the thermodynamic and dynamic mechanisms by which complex terrain can affect low-level winds. The upper easterly jet at the Maipo Canyon exit shares some features with the thermodynamically driven valley exit jet studied by CWH2013 in a similar topographical setting: preference for nighttime conditions and intensification at the canyon exit. However, it has a higher altitude above the ground, an opposite seasonal preference, and it is associated with well-defined synoptic patterns. On the other hand, the warming and drying associated with the onset of the raco wind at the surface resemble that of foehn events when parcels dynamically forced to rapidly descend by the topography produce such effects on stations downwind of a cross barrier. In the absence of a clear cross barrier in our case, however, we speculate that a gap mechanism may be acting like that described for shallow-foehn cases in the Alps by Armi and Mayr (2007). A lateral 3:1:3 constriction indeed exists in the Maipo Canyon exit corridor between La Obra and Manzano stations, which could be controlling the acceleration and descent of the flow exiting the canyon.

RG2004 showed that raco episodes occur under conditions of regional lower-tropospheric (below ~700 hPa) easterly flow intensification and warming. Furthermore, they suggested that ''strong downvalley flow within the zonally oriented Andean valleys is triggered and sustained by the regional-scale flow, being modified by local orographic effects.'' The hydraulic gap-wind hypothesis to explain the intense raco wind at the exit of the Maipo Canyon provides a concrete example of how the orographic modification suggested by RG2004 may take place. Numerical modeling to be performed in future work may help to verify the gap-wind hypothesis and, more generally, to elucidate the relative roles of the dynamic and thermodynamic forcings of the raco.

Acknowledgments. This work was partially funded by FONDECYT Projects 1131092 and 1170214 of the Chilean CONICYT agency. The sodar was acquired with funds from FONDAP Grant 15110009. Measurements at La Obra have been possible with the collaboration from Mr. Ramón Espósito from the Junta de Vigilancia del Río Maipo. Data from Guayacán station is provided by the Dirección Meteorológica de Chile. Measurements at Almenar and El Manzano were possible with the collaboration of Colegio Almenar del Maipo (Board Director Mr. Antonio Rabajille) and Escuela Básica de El Manzano (Director Ms. Catherine Echeverría), respectively. Students taking part in the field campaigns were Valentina Astudillo, Tomás Caballero, Tomás Carrasco, Vanessa Carril, Natalia Carrera, Alina Espinoza, Constanza Flores, Johana Gallardo, Jorge Gacitúa, Álvaro Gómez, Luis Gómez, Diego Hernández, Rodrigo Hevia, Camilo Márquez, Felipe Matus, Charlie Opazo, María Jesús Rapanague, Christian Segura, Constanza Urzúa, Felipe Vargas, Efraín Valencia, and Daniel Veloso. The constructive suggestions of three anonymous reviewers are acknowledged.

REFERENCES

Armi, L., and R. Williams, 1993: The hydraulics of a stratified fluid flowing through a contraction. *J. Fluid Mech.*, **251**, 355–375, https://doi.org/10.1017/S0022112093003441.

——, and G. J. Mayr, 2007: Continuously stratified flows across an Alpine crest with a pass: Shallow and deep föhn. *Quart. J. Roy. Meteor. Soc.*, **133**, 459–477, https://doi.org/10.1002/qj.22.

——, and ——, 2011: The descending stratified flow and internal hydraulic jump in the lee of the Sierras. *J. Appl. Meteor. Climatol.*, **50**, 1995–2011, https://doi.org/10.1175/JAMC-D-10-05005.1.

Arriagada, A., 2019: Observational characterization of terral events in the Pelambres River valley (in Spanish). M.S. thesis, Master Program in Meteorology and Climatology, University of Chile, 68 pp.

Baines, P. G., 1995: *Topographic Effects in Stratified Flows*. Cambridge University Press, 482 pp.

Beusch, L., S. Raveh-Rubin, M. Sprenger, and L. Papritz, 2018: Dynamics of a puelche foehn event in the Andes. *Meteor. Z.*, **27**, 67–80, https://doi.org/10.1127/metz/2017/0841.

Caicedo, V., B. Rappenglück, B. Lefer, G. Morris, D. Toledo, and R. Delgado, 2017: Comparison of aerosol lidar retrieval methods for boundary layer height detection using ceilometer aerosol backscatter data. *Atmos. Meas. Tech.*, **10**, 1609–1622, https://doi.org/10.5194/amt-10-1609-2017.

Castro, A., 2018: Numerical modeling of a raco wind event in central Chile and its sensitivity to topography (in Spanish). M.S. thesis, Master Program in Meteorology and Climatology, University of Chile, 192 pp.

Chrust, M. F., C. D. Whiteman, and S. W. Hoch, 2013: Observations of thermally driven wind jets at the exit of Weber Canyon, Utah. *J. Appl. Meteor. Climatol.*, **52**, 1187–1200, https://doi.org/10.1175/JAMC-D-12-0221.1.

De Bruin, H. A. R., B. J. J. M. Van Den Hurk, and J. M. Kroon, 1999: On the temperature-humidity correlation and similarity. *Bound.-Layer Meteor.*, **93**, 453–468, https://doi.org/10.1023/A:1002071607796.

Finn, D., and Coauthors, 2016: Evidence for gap flows in the Birch Creek Valley, Idaho. *J. Atmos. Sci.*, **73**, 4873–4894, https://doi.org/10.1175/JAS-D-16-0052.1.

Fuenzalida, H., R. Sánchez, and R. Garreaud, 2005: A climatology of cutoff lows in the Southern Hemisphere. *J. Geophys. Res.*, **110**, D18101, https://doi.org/10.1029/2005JD005934.

Garreaud, R., 2013: Warm winter storms in central Chile. *J. Hydrometeor.*, **14**, 1515–1534, https://doi.org/10.1175/JHM-D-12-0135.1.

——, and J. Rutllant, 2003: Coastal lows along the subtropical west coast of South America: Numerical simulation of a typical case. *Mon. Wea. Rev.*, **131**, 891–908, https://doi.org/10.1175/1520-0493(2003)131<0891:CLATSW>2.0.CO;2.

——, ——, and H. Fuenzalida, 2002: Coastal lows along the subtropical west coast of South America: Mean structure and evolution. *Mon. Wea. Rev.*, **130**, 75–88, https://doi.org/10.1175/1520-0493(2002)130<0075:CLATSW>2.0.CO;2.

Inzunza, J., 2009: The relation between puelche wind and the occurrence of forest fires in Bío Bío region, Chile (in Spanish). *Ing. Cienc.*, **5**, 33–48.

Jackson, P. L., G. Mayr, and S. Vosper, 2013: Dynamically-driven winds. *Mountain Weather Research and Forecasting: Recent Progress and Current Challenges*, F. K. Chow et al., Eds., Springer, 121–218.

Kalthoff, N., and Coauthors, 2002: Mesoscale wind regimes in Chile at 30°S. *J. Appl. Meteor.*, **41**, 953–970, https://doi.org/10.1175/1520-0450(2002)041<0953:MWRICA>2.0.CO;2.

Kotthaus, S., E. O'Connor, C. Münkel, C. Charlton-Perez, M. Haeffelin, A. M. Gabey, and C. S. B. Grimmond, 2016: Recommendations for processing atmospheric attenuated backscatter profiles from Vaisala CL31 ceilometers. *Atmos. Meas. Tech.*, **9**, 3769–3791, https://doi.org/10.5194/amt-9-3769-2016.

Mahrt, L., 1982: Momentum balance of gravity flows. *J. Atmos. Sci.*, **39**, 2701–2711, https://doi.org/10.1175/1520-0469(1982)039<2701:MBOGF>2.0.CO;2.

Mass, C. F., M. D. Warner, and R. Steed, 2014: Strong westerly wind events in the Strait of Juan de Fuca. *Wea. Forecasting*, **29**, 445–465, https://doi.org/10.1175/WAF-D-13-00026.1.

Mayr, G. J., and Coauthors, 2007: Gap flows: Results for the Mesoscale Alpine Programme. *Quart. J. Roy. Meteor. Soc.*, **133**, 881–896, https://doi.org/10.1002/qj.66.

——, and Coauthors, 2018: The Community Foehn Classification Experiment. *Bull. Amer. Meteor. Soc.*, **99**, 2229–2235, https://doi.org/10.1175/BAMS-D-17-0200.1.

Montecinos, A., R. Muñoz, S. Oviedo, A. Martínez, and V. Villagrán, 2017: Climatological characterization of puelche winds down the western slope of the extratropical Andes Mountains using the NCEP Climate Forecast System Reanalysis. *J. Appl. Meteor. Climatol.*, **56**, 677–696, https://doi.org/10.1175/JAMC-D-16-0289.1.

Montes, C., J. Rutllant, A. Aguirre, L. Bascuñán-Godoy, and C. Juliá, 2016: Terral de Vicuña, a foehnlike wind in semiarid northern Chile: Meteorological aspects and implications for the fulfillment of chill requirements in deciduous fruit trees. *J. Appl. Meteor. Climatol.*, **55**, 1183–1196, https://doi.org/10.1175/JAMC-D-15-0275.1.

Muñoz, R. C., and A. Undurraga, 2010: Daytime mixed layer over the Santiago Basin: Description of two years of observations with a lidar ceilometer. *J. Appl. Meteor. Climatol.*, **49**, 1728–1741, https://doi.org/10.1175/2010JAMC2347.1.

——, and M. Corral, 2017: Surface indices of wind, stability, and turbulence at a highly polluted urban site in Santiago, Chile,

and their relationship with nocturnal particulate matter concentrations. *Aerosol Air Qual. Res.*, **17**, 2780–2790, https://doi.org/10.4209/aaqr.2017.05.0190.

——, M. Falvey, M. Araya, and M. Jacques-Coper, 2013: Strong down-valley low-level jets over the Atacama Desert: Observational characterization. *J. Appl. Meteor. Climatol.*, **52**, 2735–2752, https://doi.org/10.1175/JAMC-D-13-063.1.

Norte, F. A., A. G. Ulke, S. C. Simonelli, and M. Viale, 2008: The severe zonda wind event of 11 July 2006 east of the Andes Cordillera (Argentine): A case study using the BRAMS model. *Meteor. Atmos. Phys.*, **102**, 1–14, https://doi.org/10.1007/s00703-008-0011-6.

Parish, T., and D. Bromwich, 1987: The surface windfield over the Antarctic ice sheets. *Nature*, **328**, 51–54, https://doi.org/10.1038/328051a0.

Peng, J., and Coauthors, 2017: Ceilometer-based analysis of Shangai's boundary layer height (under rain- and fog-free conditions). *J. Atmos. Oceanic Technol.*, **34**, 749–764, https://doi.org/10.1175/JTECH-D-16-0132.1.

Platis, A., A. F. Moene, D. M. Villagrasa, F. Beyrich, D. Tupman, and J. Bange, 2017: Observations of the temperature and humidity structure parameter over heterogeneous terrain by airborne measurements during the LITFASS-2003 campaign. *Bound.-Layer Meteor.*, **165**, 447–473, https://doi.org/10.1007/s10546-017-0290-x.

Richner, H. L., and P. Hächler, 2013: Understanding and forecasting Alpine foehn. *Mountain Weather Research and Forecasting: Recent Progress and Current Challenges*, F. K. Chow et al., Eds., Springer, 219–260.

Rutllant, J., and R. Garreaud, 2004: Episodes of strong flow down the western slope of the subtropical Andes. *Mon. Wea. Rev.*, **132**, 611–622, https://doi.org/10.1175/1520-0493(2004)132<0611:EOSFDT>2.0.CO;2.

Vüllers, J., G. J. Mayr, U. Corsmeier, and C. Kottmeier, 2018: Characteristics and evolution of diurnal foehn events in the Dead Sea valley. *Atmos. Chem. Phys.*, **18**, 18 169–18 186, https://doi.org/10.5194/acp-18-18169-2018.

Ward, H. C., 2017: Scintillometry in urban and complex environments: A review. *Meas. Sci. Technol.*, **28**, 064005, https://doi.org/10.1088/1361-6501/aa5e85.

Whiteman, C. D., 2000: *Mountain Meteorology: Fundamentals and Applications*. Oxford University Press, 355 pp.

——, and J. C. Doran, 1993: The relationship between overlying synoptic-scale flows and winds within a valley. *J. Appl. Meteor.*, **32**, 1669–1682, https://doi.org/10.1175/1520-0450(1993)032<1669:TRBOSS>2.0.CO;2.

Wood, I. R., 1968: Selective withdrawal from a stably stratified fluid. *J. Fluid Mech.*, **32**, 209–223, https://doi.org/10.1017/S0022112068000686.

Zardi, D., and C. D. Whiteman, 2013: Diurnal mountain wind systems. *Mountain Weather Research and Forecasting: Recent Progress and Current Challenges*, F. K. Chow et al., Eds., Springer, 35–119.